

## INFORMATION TO USERS

This reproduction was made from a copy of a manuscript sent to us for publication and microfilming. While the most advanced technology has been used to photograph and reproduce this manuscript, the quality of the reproduction is heavily dependent upon the quality of the material submitted. Pages in any manuscript may have indistinct print. In all cases the best available copy has been filmed.

The following explanation of techniques is provided to help clarify notations which may appear on this reproduction.

1. Manuscripts may not always be complete. When it is not possible to obtain missing pages, a note appears to indicate this.
2. When copyrighted materials are removed from the manuscript, a note appears to indicate this.
3. Oversize materials (maps, drawings, and charts) are photographed by sectioning the original, beginning at the upper left hand corner and continuing from left to right in equal sections with small overlaps. Each oversize page is also filmed as one exposure and is available, for an additional charge, as a standard 35mm slide or in black and white paper format.\*
4. Most photographs reproduce acceptably on positive microfilm or microfiche but lack clarity on xerographic copies made from the microfilm. For an additional charge, all photographs are available in black and white standard 35mm slide format.\*

\*For more information about black and white slides or enlarged paper reproductions, please contact the Dissertations Customer Services Department.

**UIMIC** University  
Microfilms  
International



8613992

**Hitti, Bassam Sallm**

EFFECT OF STRAIN ON MUON DIFFUSION AND TRAPPING IN METAL

*The College of William and Mary in Virginia*

PH.D. 1986

**University  
Microfilms  
International** 300 N. Zeeb Road, Ann Arbor, MI 48106



**PLEASE NOTE:**

In all cases this material has been filmed in the best possible way from the available copy. Problems encountered with this document have been identified here with a check mark ✓.

1. Glossy photographs or pages \_\_\_\_\_
2. Colored illustrations, paper or print \_\_\_\_\_
3. Photographs with dark background \_\_\_\_\_
4. Illustrations are poor copy \_\_\_\_\_
5. Pages with black marks, not original copy \_\_\_\_\_
6. Print shows through as there is text on both sides of page \_\_\_\_\_
7. Indistinct, broken or small print on several pages ✓
8. Print exceeds margin requirements \_\_\_\_\_
9. Tightly bound copy with print lost in spine \_\_\_\_\_
10. Computer printout pages with indistinct print \_\_\_\_\_
11. Page(s) \_\_\_\_\_ lacking when material received, and not available from school or author.
12. Page(s) \_\_\_\_\_ seem to be missing in numbering only as text follows.
13. Two pages numbered \_\_\_\_\_. Text follows.
14. Curling and wrinkled pages \_\_\_\_\_
15. Dissertation contains pages with print at a slant, filmed as received \_\_\_\_\_
16. Other \_\_\_\_\_  
\_\_\_\_\_  
\_\_\_\_\_

University  
Microfilms  
International



EFFECT OF STRAIN ON MUON DIFFUSION AND  
TRAPPING IN METAL

---

A Dissertation

Presented to

The Faculty of the Department of Physics  
The College of William and Mary in Virginia

In Partial Fulfillment  
Of the Requirements for the Degree of  
Doctor of Philosophy

---

by

Bassam Salim Hitti

1986

APPROVAL SHEET

This dissertation is submitted in partial fulfillment of  
the requirements for the degree of

Doctor of Philosophy



---

Bassam Salim Hitti

Approved, May 1986



---

William J. Kossler



---

Kenneth G. Petzinger



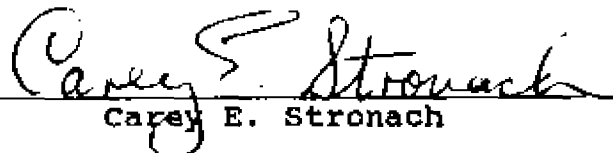
---

Harlan E. Schone



---

Mark S. Conradi



---

Carey E. Stronach

To the memory of my friend and classmate

Nicole Kuhn

## TABLE OF CONTENTS

ACKNOWLEDGEMENTS . . . . .	vi
LIST OF TABLES . . . . .	vii
LIST OF FIGURES . . . . .	ix
ABSTRACT . . . . .	xi
chapter	page
I INTRODUCTION . . . . .	2
II MUONS . . . . .	5
2.1 PRODUCTION . . . . .	5
2.2 DECAY . . . . .	7
2.3 DETECTION and DATA COLLECTION. . . . .	9
III MUONS INTERACTIONS IN METALS . . . . .	15
3.1 MAGNETIC INTERACTION . . . . .	16
A. Introduction to Magnetism . . . . .	16
B. Muon Nuclei Interaction in Diamagnetic Metal . . . . .	18
C. Muon as a Microscopic Probe of Magnetism . . . . .	18
D. Action of a Uniform Field on the Muon Spin . . . . .	21
E. Transverse Field $\mu$ SR . . . . .	21
F. Zero and Longitudinal Field $\mu$ SR . . . . .	29
3.2 ELECTRONIC INTERACTION . . . . .	33
3.3 ELASTIC INTERACTION . . . . .	38
A. Elastic Compliance and Stiffness Constants . . . . .	38
B. Distortions Around a Point Defect . . . . .	39
C. Interaction Between Two Point Defects . . . . .	43
D. Muon-Uniaxial Stress Interaction . . . . .	44
E. Conclusion . . . . .	46

IV	DIFFUSION AND TRAPPING IN AL(IMPURITY) ALLOYS	47
4.1	OVERVIEW	47
4.2	SYMMETRY BREAKING	52
4.3	EXPERIMENT, RESULTS and INTERPRETATION	56
A.	Fitting	56
B.	Samples	56
C.	AlCu <sub>420</sub> ppm	56
D.	AlMg <sub>1000</sub> ppm	62
E.	AlAg <sub>1000</sub> ppm	69
4.4	SUMMARY	69
V	UNIAXIAL STRESS-INDUCED SYMMETRY BREAKING OF MUON SITES IN IRON	72
5.1	OVERVIEW	72
5.2	EXPERIMENT	77
A.	Samples	77
B.	Beams	77
C.	Pulling Apparatus	78
D.	Temperature	78
E.	Strain	80
F.	Data Analysis	81
G.	Magnetic Domain Alignment	82
5.3	RESULTS and DISCUSSION	86
5.4	SUMMARY	93
VI	CONCLUSION	97
	APPENDIX	
A.	Z-Component of Nuclear Dipolar Field	98
B.	Two State Model	99
	REFERENCES	100

## ACKNOWLEDGEMENTS

I am grateful for all the help, support and friendship I have received in the past five years from the faculty, staff and graduate students of the physics department at the College of William and Mary.

I wish to express my appreciation to Professor William J. Kossler for setting up the equipment, hard work while the experiments were running and his guidance during data analysis.

I am also indebted to the members of my committee Professors Kenneth G. Petzinger, Harlan E. Schone, Mark S. Conradi and Carey E. Stronach for reading the manuscript and for their help in many other ways.

Finally I wish to thank James Kempton for his part in the experiments, Terry Gullion, Su-Huai Wei and Betru Debebe for their friendship.

## LIST OF TABLES

	page
2.1 Characteristics of the stopping muon beam at Brookhaven National Laboratory . . . . .	13
2.2 Muon properties relevant to Muon Spin Rotation . . . . .	14
3.1 Magnetic dipole moments due to the spins of electrons, protons and neutrons . . . . .	17
4.1 Aluminum data . . . . .	49
4.2 Lattice dilation in Al due to substitutional and interstitial impurities. Also listed are the impurities' spins and magnetic moments . . . . .	54
4.3 Results of zero and 14.2G longitudinal experiment on AlCu <sub>420</sub> ppm . . . . .	60
4.4 Calculated values of the static second moment of the random fields in Al for the case of zero external field . . . . .	61
4.5 Transverse field results on AlMg . . . . .	63
4.6 The static second moment of the random fields in Al for a strong external transverse field . . . . .	65
5.1 Properties and $\mu$ SR results of Iron (Fe) . . . . .	75
5.2 $C_{11}$ and $C_{12}$ for Fe at 298K, 373K and 360K are listed. $S_{11}$ and $S_{12}$ are calculated . . . . .	80
5.3 Stress-Strain in the <100> direction for Fe(3 wt. % Si) . . . . .	81
5.4 Results of $\mu$ SR measurements on Fe and Fe(3 wt. % Si). Change in frequency and field with strain and temperature . . . . .	86
5.5 The dipolar field at muon sites in Fe under various conditions at T=0K . . . . .	90

5.6	Extrapolation of the difference between the diagonal elements of the double force tensor from Nb to Fe for muons at O(T) sites . . . .	91
5.7	Comparison of the change in the local field sensed by muons from first principle calculations and from Nb extrapolations to the experimental result. . . . .	92

## LIST OF FIGURES

	page
2.1 The muon beam line at the AGS at BNL . . . . .	6
2.2 The positron probability distribution around the muon spin upon decay . . . . .	8
2.3 The $\mu$ SR apparatus at BNL . . . . .	11
2.4 The logic diagram of the $\mu$ SR set up at BNL . . . . .	12
3.1 The origins of $B_{dem.}$ and $B_L$ at a muon site in a ferromagnet . . . . .	20
3.2 The action of an external field H on the muon spin S . . . . .	22
3.3a A forward $\mu$ SR spectrum taken at BNL on AlMg at 10K and a transverse field of 150G . . . . .	24
3.3b A forward $\mu$ SR spectrum taken at BNL on AlMg at 295K and a transverse field of 150G . . . . .	25
3.4 A representation of the angles used to express the z component of the nuclear dipolar field . . . . .	28
3.5 Zero field data taken at BNL on AlMg at 10K . . . . .	30
3.6 Various types of lattices of interstitial sites in FCC and BCC lattices . . . . .	34
3.7 Self consistent electron density around a proton in Al . . . . .	36
3.8 Change in the energy of a muon at nearest and second nearest T sites to a substitutional impurity with respect to a T site in pure Al . . . . .	37
3.9 The Kanzaki forces . . . . .	40
4.1 Expected behaviour of the damping parameter of the $\mu$ SR signal for metal as a function of temperature . . . . .	48

4.2a	Damping parameter for AlMn . . . . .	50
4.2b	Damping parameter for deformed Al,AlMg,AlCu and AlZn . . . . .	51
4.3	Lattice spacings of Al solid solutions as a function of composition . . . . .	53
4.4	Muon polarization as a function of temperature for AlCu <sub>420ppm</sub> . . . . .	58
4.5	The trapping and escape rates versus temperature for AlCu . . . . .	59
4.6	The damping parameter versus temperature from BNL on AlMg at 150G transverse field . . . . .	64
4.7	A plot of $\ln\tau_c$ versus $1/kT$ . . . . .	66
4.8	Polarization versus time, the curves are for a static field surrounding at zero and 7G longitudinal field, the data are from BNL on AlMg and AlAg . . . . .	67
5.1	Possible muon sites in an Fe lattice and the difference in their dipolar field . . . . .	73
5.2	The saturation magnetization versus temperature for pure Fe . . . . .	76
5.3	The pulling apparatus . . . . .	79
5.4	Precession frequency versus applied field . . . . .	83
5.5	The ratio $F_t/F_l$ (measure of domain alignment) versus applied field for pure Fe . . . . .	84
5.6	Depolarization rate for Fe(3 wt. % Si) versus applied field . . . . .	85
5.7	Precession frequency for (a) pure Fe at 300K (b) Fe(3 wt. % Si) at 300K and (c) Fe(3 wt. % Si) at 360K versus strain . . . . .	87
5.8a	$\mu$ SR data from Fe(3 wt. % Si) taken at 360K . . . . .	94
5.8b	$\mu$ SR data from Fe(3 wt. % Si) taken at 215K . . . . .	95
5.9	The depolarization as a function of temperature for the Fe(3 wt. % Si) . . . . .	96

## ABSTRACT

Positive muons implanted in metal distort the surrounding lattice; therefore, in addition to electronic interactions, the elastic forces have to be considered in determining the muon state. To explore the elastic and electronic diffusion and trapping mechanisms, we studied AlCu<sub>420ppm</sub>, AlMg<sub>1000ppm</sub> and AlAg<sub>1000ppm</sub> alloys. These alloys were selected for the different effects on the host lattice of these impurities; Cu contracts the Al lattice, Mg expands it and Ag has nearly no effect. On the other hand Cu and Ag are monovalent while Mg is divalent. For AlCu between 5K and 14K the temperature exponent  $\beta$  of the two-state-model trapping rate ( $\nu_0 T^\beta$ ) was  $0.93 \pm .26$  for zero field and  $1.16 \pm .14$  for a 14.2G longitudinal field. A  $\beta$  of 1 implies a one phonon induced diffusion process. For AlMg the transverse field (150G) second moment of the static random fields was  $0.317 \pm .007 \mu\text{s}^{-1}$  between 10K and 60K,  $0.221 \pm .013 \mu\text{s}^{-1}$  between 60K and 150K and  $0.150 \pm .013 \mu\text{s}^{-1}$  between 150K and 300K. The changing value of the second moment indicates a change in the muon trapping site from tetrahedral to octahedral to vacancy as the temperature is increased, this was confirmed at appropriate temperatures by zero and longitudinal field studies. Comparing the AlMg results with earlier work on AlCu two types of trapping sites can be identified, those dependent on the magnitude but not sign of deformation, and thought to be a few atomic distances away from the defect, and those which are possibly close to Mg. For AlAg, since Ag has almost no elastic effect the weaker depolarization structure suggests a different trapping mechanism, possibly due to the electronic interaction. To study the muon interaction with a uniform strain field, uniaxial stress was applied to an Fe(3 wt. % Si) single crystal. We measured the temperature dependence of the frequency shift versus strain to be  $-0.348 \pm .007 \text{ MHz}/100\mu\epsilon$  ( $25.7 \pm .5 \text{ G}/100\mu\epsilon$ ) at 300K and  $-0.279 \pm .010 \text{ MHz}/100\mu\epsilon$  ( $20.6 \pm .7 \text{ G}/100\mu\epsilon$ ) at 360K. The agreement of the room temperature result with earlier work on pure Fe shows that these shifts are inherent to Fe and not impurity dependent. That the shifts are proportional to  $(1/T)$  confirms that these effects are dominated by a strain-induced-muon-population shifts between crystallographically equivalent but magnetically inequivalent sites.

EFFECT OF STRAIN ON MUON DIFFUSION AND  
TRAPPING IN METAL

## INTRODUCTION

Muon Spin Rotation ( $\mu$ SR) has developed in the last ten years into a technique for the study of chemistry, semiconductor physics, alloys, magnetic and electronic properties of metals and diffusion of light particles in solids<sup>1,2</sup>. More recently it has been applied to metal hydrides and heavy fermion systems.

The muons' exotic nature shows up only in their creation and decay<sup>3</sup> (chapter 2). The interactions with their local environment are determined by their charge and spin. In the time differential technique positive muons are stopped one at a time in the sample, and are therefore considered to be charged impurities in extreme dilution. Three questions of interest related to muons in metals are:

- 1) How does a muon interact with and disturb the surrounding?
- 2) How does it diffuse and where does it go once stopped in the sample?
- 3) What can be learned about the material itself?

The interactions of a positive muon in a metal can be divided into magnetic, electronic and elastic parts. The origins of these forces are interconnected, but this division leads to a simplified description of the physical situation. The magnetic interaction determines what can be learned about the system, while the electronic and elastic forces determine

how the muon disturbs the lattice, how it moves, and where it goes.

This work is a study of the effect of strain on muons in metals. The distortion field around a muon can be described as an elastic dipole<sup>17,35</sup> and the interaction of this dipole with other point defects (dipole-dipole interaction) or with a uniform stress field (dipole-uniaxial stress interaction) were investigated in two experiments we performed at Brookhaven National Laboratory (BNL). A positive muon in metal can be considered as a light isotope of hydrogen ( $m_\mu = 0.11 m_p$ ). Its interaction with point defects, external or internal (crack) stress fields, provide information on hydrogen behaviour. Hydrogen implanted in a metal causes changes in the metal physical properties and may lead in some cases to serious technological problems such as hydrogen embrittlement.

In the first set of experiments point defects with different local effects on the host Al lattice were used. These defects break the symmetry between possible muon sites splitting their degenerate energy levels. The elastic interaction of a muon and an impurity atom in a crystal has not been theoretically calculated. Here we use the results of continuum theory to describe the long range forces<sup>4</sup>, while the results of lattice static (sums over metal atoms) calculations for hydrogen-substitutional impurity interaction in body centered cubic (Nb,V,Ta) metals were used for the short range interaction<sup>5</sup>. Both results can be expressed in

terms of the double force tensor<sup>6</sup> which is related to the local deformation around the impurity in the lattice (section 3.3). Combining the above with the pseudopotential calculations for trapping of muons by impurities in Aluminum<sup>7</sup> (section 3.2), we present in chapter 4 a qualitative picture of diffusion and trapping in Al(Impurity) systems.

The stress induced splitting of degenerate muon energy levels in a crystal can also be seen in another system where the analysis is simpler and can be given in a quantitative form. In this case the elastic interaction between the muons' double force tensor in Iron and an externally applied uniaxial stress field (section 3.3), results in an observable muon-precession-frequency shift. We measured the temperature dependence of the frequency shift and verified that it is due to a stress-induced change in the population of magnetically inequivalent sites (chapter 5).

In chapter 2 the muon production, decay and detection system used at BNL are described. Chapter 3 starts with a short review of magnetism and its relevance for the transverse and longitudinal field  $\mu$ SR techniques and discusses the electric and elastic interactions. The experimental details and results are given in chapter 4 for the Al(Impurity) and chapter 5 for the uniaxial-stress experiments.

## Chapter II

### MUONS

#### 2.1 PRODUCTION<sup>3</sup>

Various reactions in high energy protons will produce pions. Among these



Pions decay in a mean life time of  $2.6 \times 10^{-8}$  s according to the following parity violating weak reaction.



Because of parity violation, the muon is forced to have its spin opposite to its momentum.

In flight decay: Pions leaving the production target are guided by dipole and quadrupole magnets into a strong focussing quadrupole channel where they decay (Fig. 2.1). The muons accepted by the beam transport system are emitted to forward and backward in the pion Center of Mass (CM) frame. Backward muons (CM) will have forward polarization and lower momentum in the laboratory frame compared to the backward polarized forward emitted muons. The

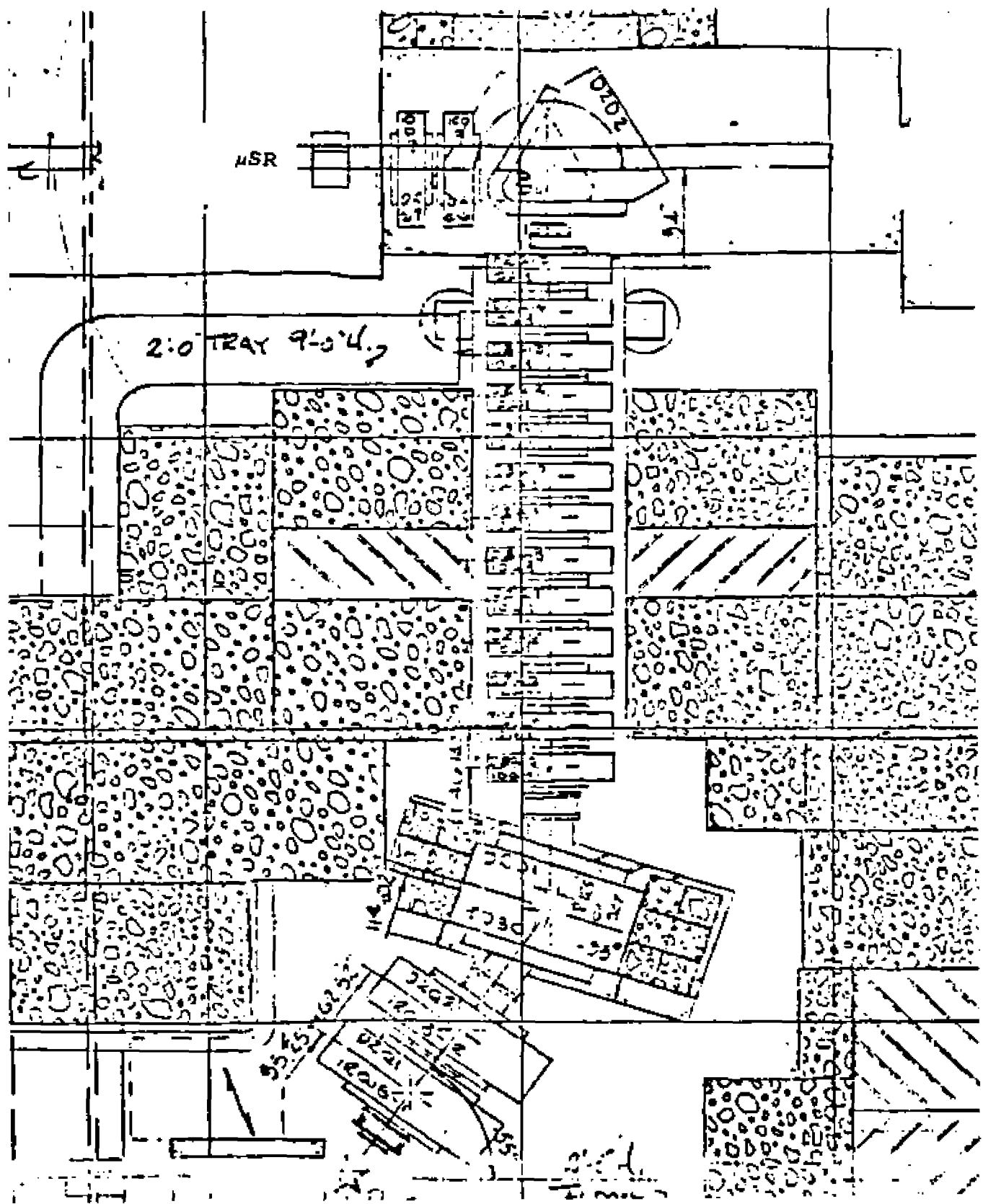


Figure 2.1  
The muon beam line at the AGS at BNL.

characteristics of the muon beam at BNL (table 2.1) and a summary of the properties of positive muons (table 2.2) are given at the end of this chapter.

Surface muons: These muons are produced from pions decaying at rest near the surface of the production target. The momentum of these surface muons is nearly 29 MeV/c and they are almost 100 % polarized. Because of their low energy (about 4 MeV) it is important to have vacuum from the target to the sample. The advantage of low energy muons is that they can be stopped in thin samples, their disadvantage is need for a vacuum transport system and very thin defining counters.

## 2.2 DECAY

Muon Spin Rotation is made possible by the parity violating decay of the muons,



with a life time of  $2.19713 \times 10^{-6}$  s.

The angular distribution of the positrons is anisotropic with respect to the muon spin direction at the time of decay. This distribution is given by<sup>3</sup>,

$$W(\theta) = 1 + a \cos(\theta) \quad (2.4)$$

where  $\theta$  is the angle between the muon spin and the

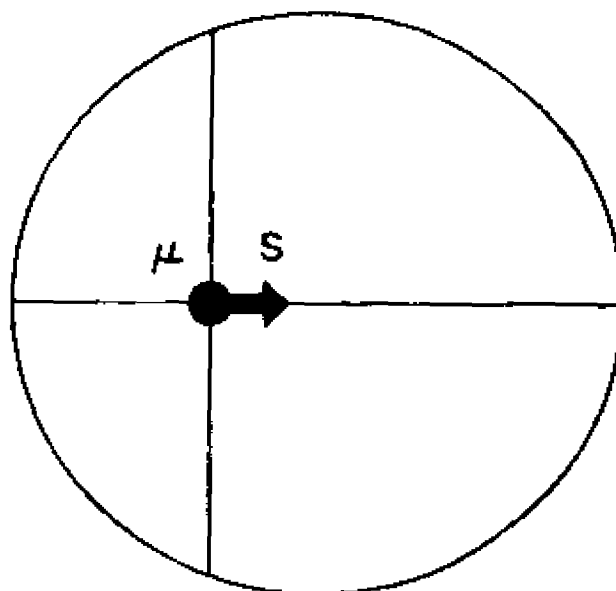


Figure 2.2

$W(\theta) = 1 + a \cos\theta$ , where  $W$  is the probability of a positron being emitted in a certain direction  $r$ ,  $\theta$  is the angle between  $r$  and the muon spin at the time of decay and  $a$  the decay asymmetry, equals  $1/3$  in the diagram and less than that in practice.

direction of the emitted positron, and  $a$  is the decay asymmetry which has a value of  $1/3$  when all positron energies are included (Fig. 2.2). In practice the beam polarization is not 100 %, and the positron detectors are of finite size. Therefore the measured asymmetry is less than  $1/3$ .

### 2.3 DETECTION and DATA COLLECTION

The  $\mu$ SR detection system used at the Alternating Gradient Synchrotron AGS at Brookhaven National Laboratory is sketched in Fig. 2.3. The detectors consist of a scintillator coupled to a photo multiplier tube via a long light guide. Detectors A3,A4,M5,F6,F7 and F8 are mounted on a table that slides so that they may go in and out of the Helmholtz coils allowing easy access to the cryostat (the rectangle between M5 and F6).

The incoming muon, after passing through a variable water degrader placed in Q17 (Fig. 2.1), are detected by M5. F6 is used to reject muons that have not stopped in the sample. Positron telescopes are placed in the forward (F7,F8) and backward (A3,A4) directions. The holes in the backward positron detectors are provided to let through incoming muons without being detected, while the holes in the forward detectors are there for reasons of symmetry. Detectors 1 and 2 are used to detect all particles coming toward the  $\mu$ SR apparatus.

A logic diagram of the electronics used at BNL for data collection is given in Fig. 2.4. Each detector

provides a logic pulse 20 ns wide, detectors 2, A4 and F7 also provide fast timing pulses of  $\approx 2$  ns width. The incoming muon is defined by  $1 \cdot 2_t \cdot M5$  and stopped muons by the following combination  $1 \cdot 2_t \cdot M5 \cdot \overline{F6}$ . Backward and forward positrons respectively are defined by  $\overline{2} \cdot A3 \cdot A4_t \cdot \overline{F7} \cdot \overline{F8}$  and  $\overline{2} \cdot F7_t \cdot F8 \cdot \overline{A3} \cdot \overline{A4}$ . The  $\mu^+$ -stop provides the start signal to a Time to Amplitude Converter (TAC), the stop signal comes from either a backward or forward positron. To ensure that the detected positron is associated with a particular muon stopped in the sample, pile-up conditions are set to inhibit and reset the TAC whenever two muons or two positrons are detected within a certain time window of each other typically 10, 15 or 20  $\mu$ s. The TAC output goes into a Multi Channel Analyzer (MCA), which sorts the muon events into a number of time bins of typically 12  $\mu$ s range. A router is used to send the forward and backward time histograms to separate memory sections of the MCA. At the end of each run the data are transferred to a PDP11 computer, stored and analyzed.

Other techniques of data collection that exploit the time structure of the particular proton accelerator are available. At KEK (Japan) the pulsed beam method is used; this implies a large number of muons entering the sample over a short period of time (beam pulse); events are timed with respect to the beam pulse, this avoids the individual timing of events. At SIN (Switzerland) the stroboscopic technique is used; this implies the determination of a frequency ratio and does not require measurement of time intervals.

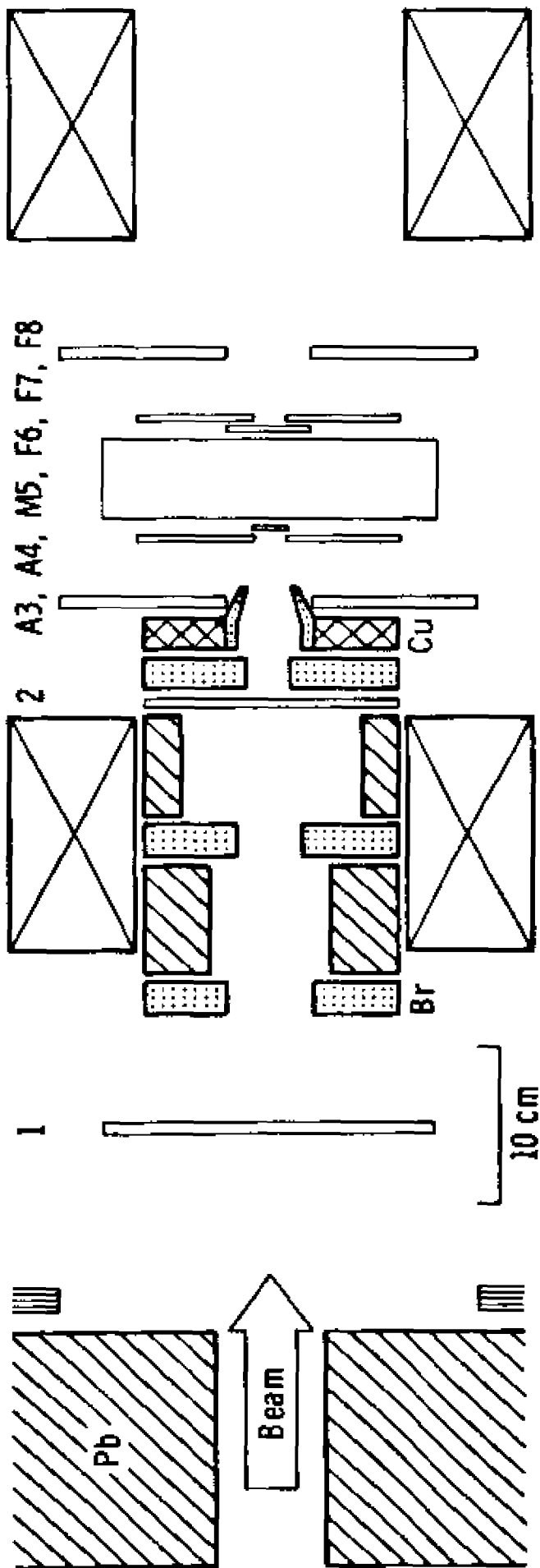


Figure 2.3  
 The  $\mu$ SR apparatus at BNL. The rectangle is the cryostat where the sample is placed and its temperature controlled. The four crossed rectangles represent the Helmholtz coils. Also shown are the detectors and collimation.

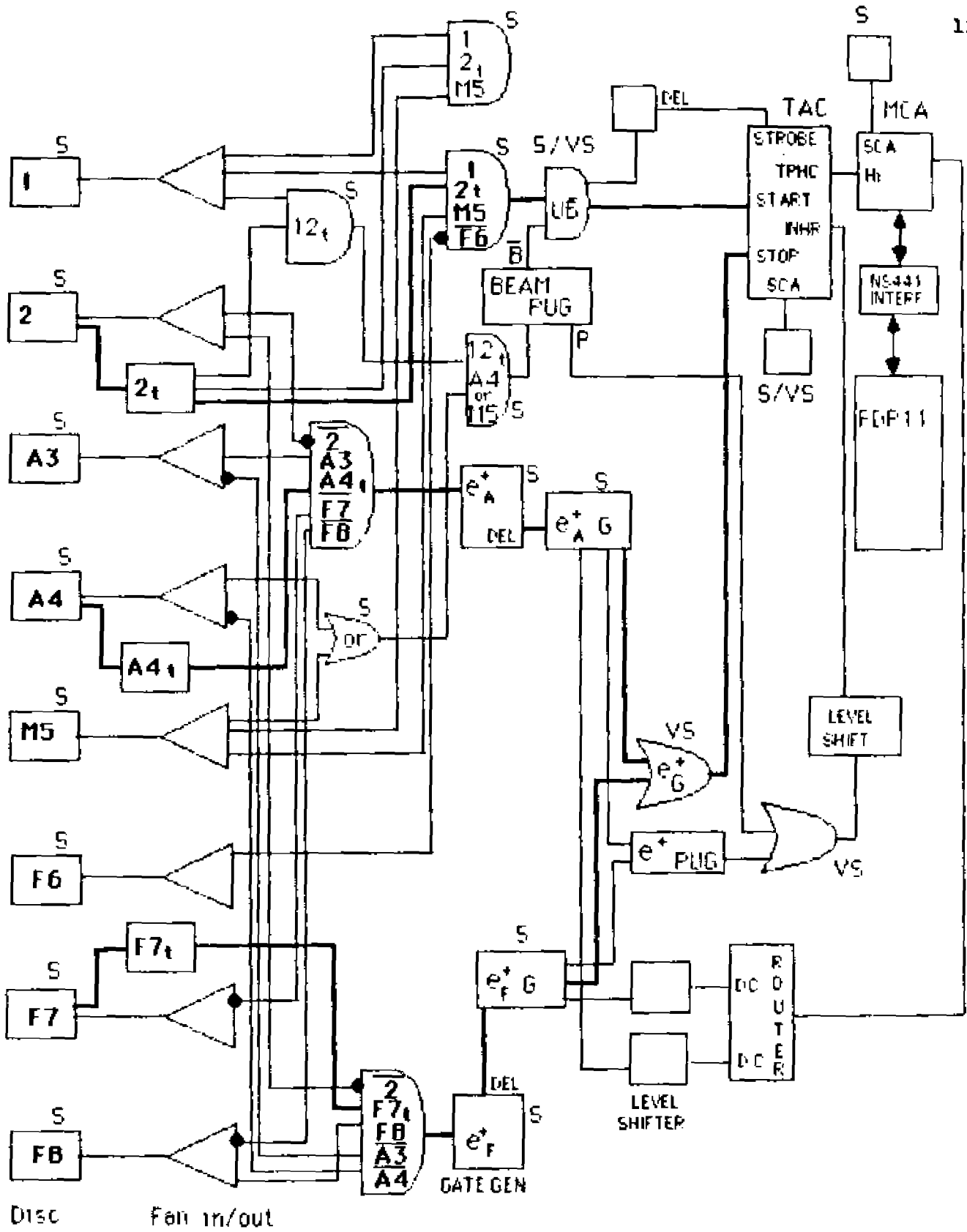


Figure 2.4  
 The logic diagram of the electronics used at BNL.

TABLE 2.1

Characteristics of the stopping muon beam at BNL

---



---

Target	7.5 x 1 x 1 cm <sup>3</sup> Pt
P <sub>π</sub>	180 MeV/c
P <sub>μ</sub>	90 MeV/c
E <sub>μ</sub>	33 MeV
Range (μ <sup>+</sup> )	5.5 grams/cm <sup>2</sup>
Maximum stopping rate with strong collimation	3 x 10 <sup>3</sup> μ <sup>+</sup> /(cm <sup>2</sup> TP*)
Polarization	80 %
Duty factor	40 %
Macro-time structure	
spill	1.5 s
acceleration	1.5 s
period	3 s
Background	0.13 %
e <sup>+</sup> (detected/muon)	0.5

---

\*TP Tera (10<sup>12</sup>) Protons at target

TABLE 2.2

Muon properties relevant to  $\mu$ SR

---



---

Production	$\pi^+ \rightarrow \mu^+ + \nu_\mu$
Decay	$\mu^+ \rightarrow e^+ + \nu_e + \bar{\nu}_\mu$
Decay asymmetry	$W(\theta) = 1 + a \cos(\theta)$
Mass	$105.66 \text{ MeV}/c^2 = 0.1126 m_p$
Spin	$1/2 \hbar$
Magnetic moment	$8.8904 \mu_N = 3.1833 \mu_p$
Gyromagnetic ratio	$13.55 \text{ kHz/G}$
Life time	$2.197 \times 10^{-6} \text{ s}$

---



---

## Chapter III

### MUON INTERACTIONS IN METALS

Muons thermalize in metals by ionization and inelastic collisions with conduction electrons,  $E_{\mu} \approx kT$ , in a time on the order of  $10^{-10}$  s or less, so that at the beginning of the  $\mu$ SR observation the muon is expected to be in a stable state characteristic of the material and the temperature determined by the muon's interaction with its surroundings.

Muonium ( $\mu^+e$ ) has not been found in metals. This is attributed to the screening of the muon by the conduction electrons. The positive muon's interaction with the lattice can be divided into three parts: electronic, elastic and magnetic. This division is artificial in the sense that the origin of magnetism is moving charges, and that of the elastic interaction is the electrostatic repulsion of atoms around the muon or impurity. The magnetic interaction determines what can be learned about the muon-host lattice system, while the electronic and elastic interactions determine where the muon goes in the lattice.

In this chapter the above three interactions will be discussed and some results relevant to  $\mu$ SR and the experiments of chapters 4 and 5 will be derived.

### 3.1 MAGNETIC INTERACTION

#### A. Introduction to Magnetism<sup>8,9</sup>

Magnetism originates from the magnetic moment due to the rotational motion of charged particles. The magnetic moment of an electron is due to two types of motion, orbital and spin. The orbital moment is

$$u = -(e/2m_e c) L \hbar, \quad (3.1)$$

where the angular momentum  $L$ , is given in units of the Planck's constant  $\hbar$ , the magnetic moment is measured in units of the Bohr magneton:

$$u_B = (e/2m_e c) \hbar = 0.917 \times 10^{-20} \text{ erg/G} \quad (3.2)$$

The magnetic moment due to the spin of an electron (spin= $S \hbar$ ) is given by,

$$u = -2 u_B S \quad (3.3)$$

The factor of two results from Dirac relativistic quantum mechanics. The above equations also hold for a collection of electrons (as in an atom) with  $L$  and  $S$  now being replaced by the total angular momentum and spin respectively.

The total magnetic dipole moment of a nucleus is the sum of the moments associated with the spin ( $1/2$ ) of the

TABLE 3.1

Magnetic dipole moments due to the spin of e, p and n<sup>10</sup>.

---



---

	Expected (Classical Theory)	Experimentally
Electron	- 1/2 u <sub>B</sub>	-1.00 u <sub>B</sub> (Dirac)
Proton	1/2 u <sub>N</sub>	2.79 u <sub>N</sub> QCD
Neutron	0	-1.91 u <sub>N</sub> QCD

---

protons and neutrons (table 3.1) and the moments of the orbital motion of the protons. The unit of nuclear magnetic moment is the Nuclear Bohr magneton, given by

$$u_N = (e/2M_p c) \hbar = 5.05 \times 10^{-24} \text{ erg/G} \quad (3.4)$$

In an atom or ion both the electrons and nucleus contribute to magnetism. An incomplete shell may have a net angular momentum and hold a stable moment (paramagnetism) given by

$$u = -u_B (L + 2S) \quad (3.5)$$

This effect when present dominates other contributions to the magnetism of an atom. A closed shell has only diamagnetism, a magnetic moment weaker than the paramagnetic moment

induced antiparallel to an applied magnetic field.

In diamagnetic metals the valence electrons are in quantum states that spread over the entire crystal. Therefore the angular momentum and magnetic moment which exists for an isolated atom are quenched for Bloch waves. A muon stopped in such a sample is subject to various effects from the surrounding nuclei.

#### B. Muon-Nuclei Interaction in Diamagnetic Metal

In diamagnetic metals the following muon-nucleus interactions have the dominant effect on the muon depolarization:

- 1- Dipole-dipole interaction ( $I \geq 1/2$ )
- 2- Interaction between the nuclear electric quadrupole moment ( $Q$ ) ( $I \geq 1$ ) and Electric Field Gradient EFG ( $q$ ) due to the positive muon ( $e q Q$ ).

The static depolarization rate can be calculated from the second moment of the random dipolar field given by Van Vleck; (sections 3.1E and 3.1F) it usually corresponds to a magnetic field of several gauss.

#### C. Muon as a Microscopic Probe of Magnetism<sup>11</sup>

Unlike the case of para- or dia- magnetic substances, spontaneous magnetic order occurs for some materials in the absence of an external field. This magnetization may not manifest itself in an overall macroscopic magnetization of the substance. A specimen may be divided into a number

of magnetic domains. The existence of spontaneous magnetism implies that the microscopic magnetic moments in a domain are aligned in one direction by the mutual interactions between the carriers of the moments, and a long range order is achieved. At high temperature, this order is destroyed and ferromagnetism changes into paramagnetism.

The electrons of the outer shell of ferromagnetic metals, such as Fe, Ni and Co are usually 4s and 3d electrons. Of these, the electrons which contribute to magnetism are mostly the 3d electrons, and it is assumed that they are in nearly atomic states.

Muons will probe the local magnetic field  $B_u$  at an interstitial site. In ordered magnetic materials there is often a strong spin polarization of the conduction electrons, induced by the local magnetic moments. Therefore the local field may be written as,

$$B_u = B_{\text{ext.}} + B_{\text{dip.}} + B_{\text{hf.}} \quad (3.6a)$$

where

$$B_{\text{dip.}} = B_{\text{dem.}} + B_L + B_{\text{dip.}}' \quad (3.6b)$$

$B_{\text{ext.}}$  is the applied external field,  $B_{\text{dem.}} = -N M$  is the shape dependent demagnetization field ( $M =$  bulk magnetization density)  $B_L = (4\pi/3) M_B$  is the lorentz field in a domain ( $M_B$  is the saturation magnetization density of a domain) and  $B_{\text{hf.}} = (-8\pi/3) \mu_B \rho_{\text{spin}}(R_u)$  is the hyperfine field due to the polarized-conduction-electron density at the

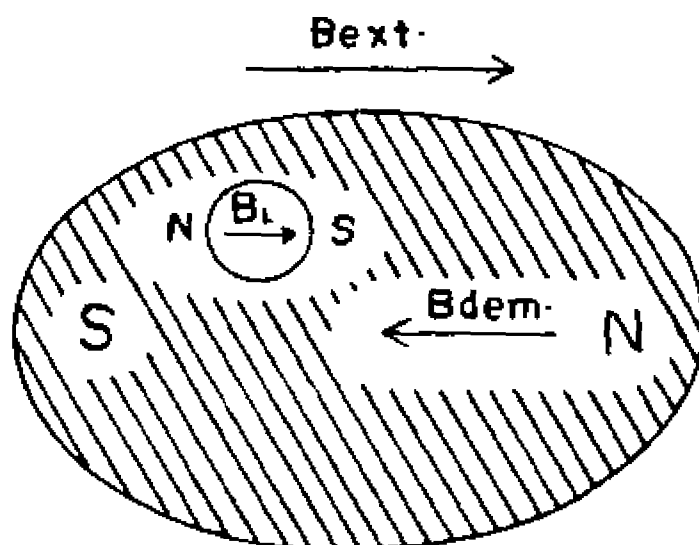


Figure 3.1

The origins of  $B_{dem}$  and  $B_L$  at a muon site in a ferromagnet are indicated. The demagnetizing field is shape dependent and arises from dipoles far from the muon.  $B_{dip}$  is due to dipoles within the Lorentz sphere while  $B_{hf}$  results from the polarized conduction electron cloud at the muon site.

muon site. Finally  $B_{dip}$  is the dipolar field from dipoles within the Lorentz sphere, its value for a static muon depends on where the muon is in the lattice, if the muon is hopping between magnetically inequivalent sites then an average depending on the mean time of stay at each site must be used.

#### D. Action of a Uniform Field on the Muon Spin

A uniform field  $H$  applies torque to rotate a dipole  $u$  equal to  $u \times H$ . If the dipole results from spin angular momentum ( $=S \hbar$ ) then it can be written as,

$$u = 2 \mu_B S. \quad (3.7)$$

Using Newton's law we can write the change in the angular momentum as,

$$\hbar dS/dt = \text{Torque} = u \times H = \omega \times S \hbar \quad (3.8)$$

therefore the action of a uniform field on such a dipole is to cause the moment to precess around  $H$  with the angular frequency  $(2\mu_B/\hbar) H$  (Fig. 3.2).

#### E. Transverse Field $\mu SR$

The Helmholtz coils, four crossed rectangles in Fig. 2.3, produce a magnetic field perpendicular to the beam direction. The spin of the muons stopping in the

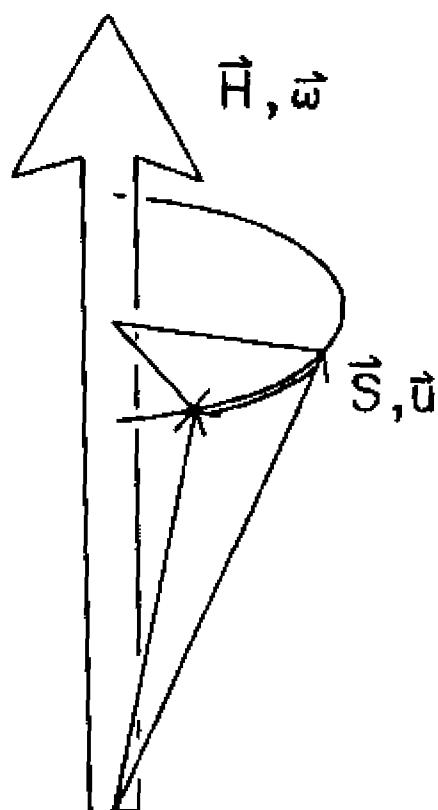


Figure 3.2

The muon a positive charge with spin  $S$  has a magnetic dipole moment  $\mu$ . An external field  $H$  will cause the muon spin to precess around  $H$  with the Larmor angular frequency  $\omega$ .

sample precess in the local magnetic field with the Larmor frequency,

$$\omega = (2\mu/\hbar) B = 2 \pi \gamma B \quad (3.9)$$

where  $\gamma$  is the gyromagnetic ratio = 13.55 kHz/G.

Since the muon decay is asymmetric, more positrons come out in the direction of the spin at the time of decay (Fig. 2.2), the time histogram (positron detected) has an oscillating part (Fig. 3.3a,b). The fitting function used to describe such histograms is,

$$N(t) = N_0 \text{EXP}(-t/\tau_\mu) (1 + P_X(t) a \text{COS}(\omega t + \phi)) + \text{Bkgd.} \quad (3.10)$$

This function is a superposition of the muon decay probability and the oscillating part mentioned above. The oscillations have the Larmor frequency  $\omega$  and an initial amplitude that reflects the asymmetry  $a$ . The damping is due to depolarization  $P_X(t)$  which results from the nonhomogeneous local magnetic fields in the sample. The parameter  $\phi$  is a phase factor which corresponds to the angle between the muon spin and the positron detectors at time zero, in the setup at BNL (Fig. 2.3),  $\phi$  is 0 for the forward (Fig. 3.3a,b) and  $\pi$  for the backward spectra.

The information about the muon environment is contained in  $\omega$  and  $P_X(t)$ . The rate of muon precession  $\omega$ , gives the local magnetic field, including any external, local

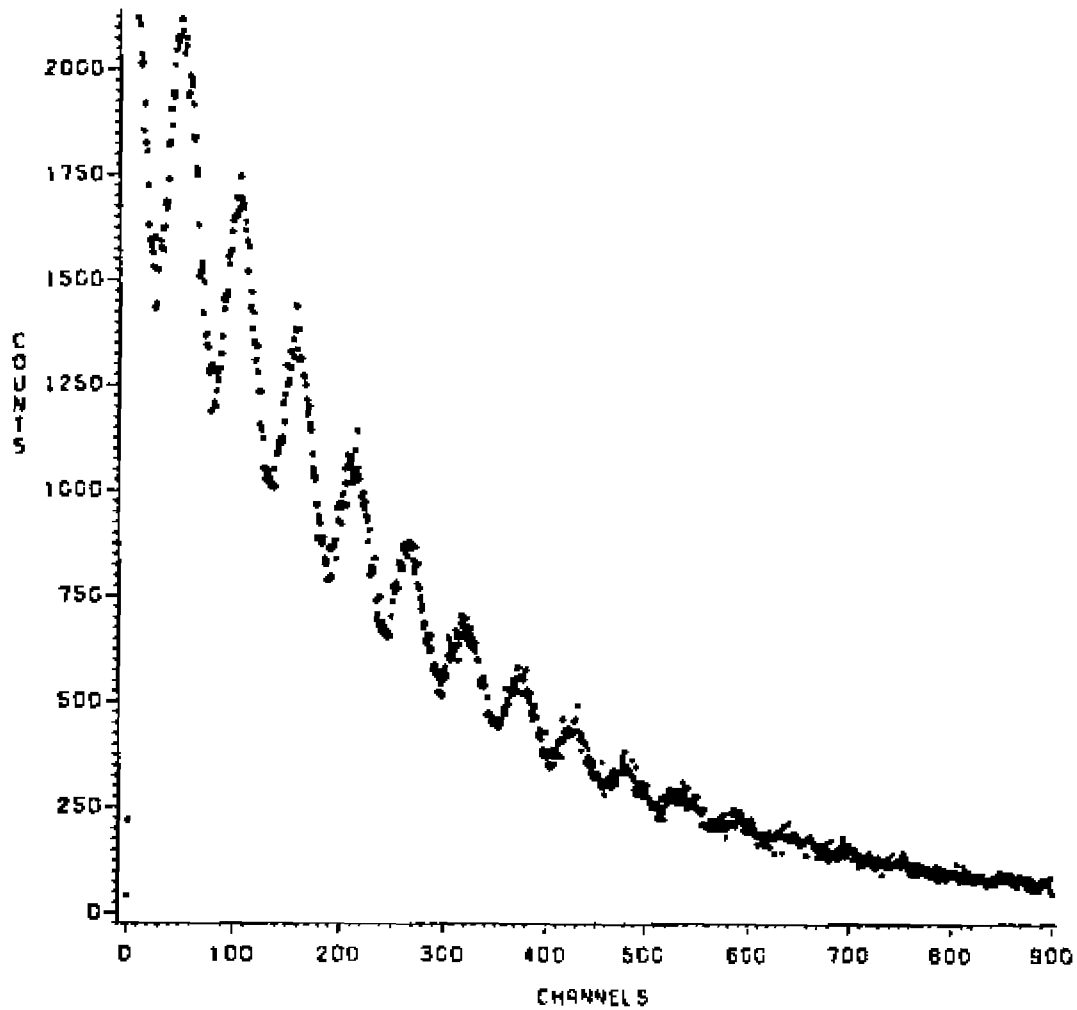


Figure 3.3a

A forward positron spectrum from BNL data on AlMg at 10K and a transverse field of 150G. There are 117.9 channels per one  $\mu\text{s}$ . The asymmetry is ( $a = 0.2$ ) and the damping parameter ( $\sigma = 0.203 \mu\text{s}^{-1}$ ).

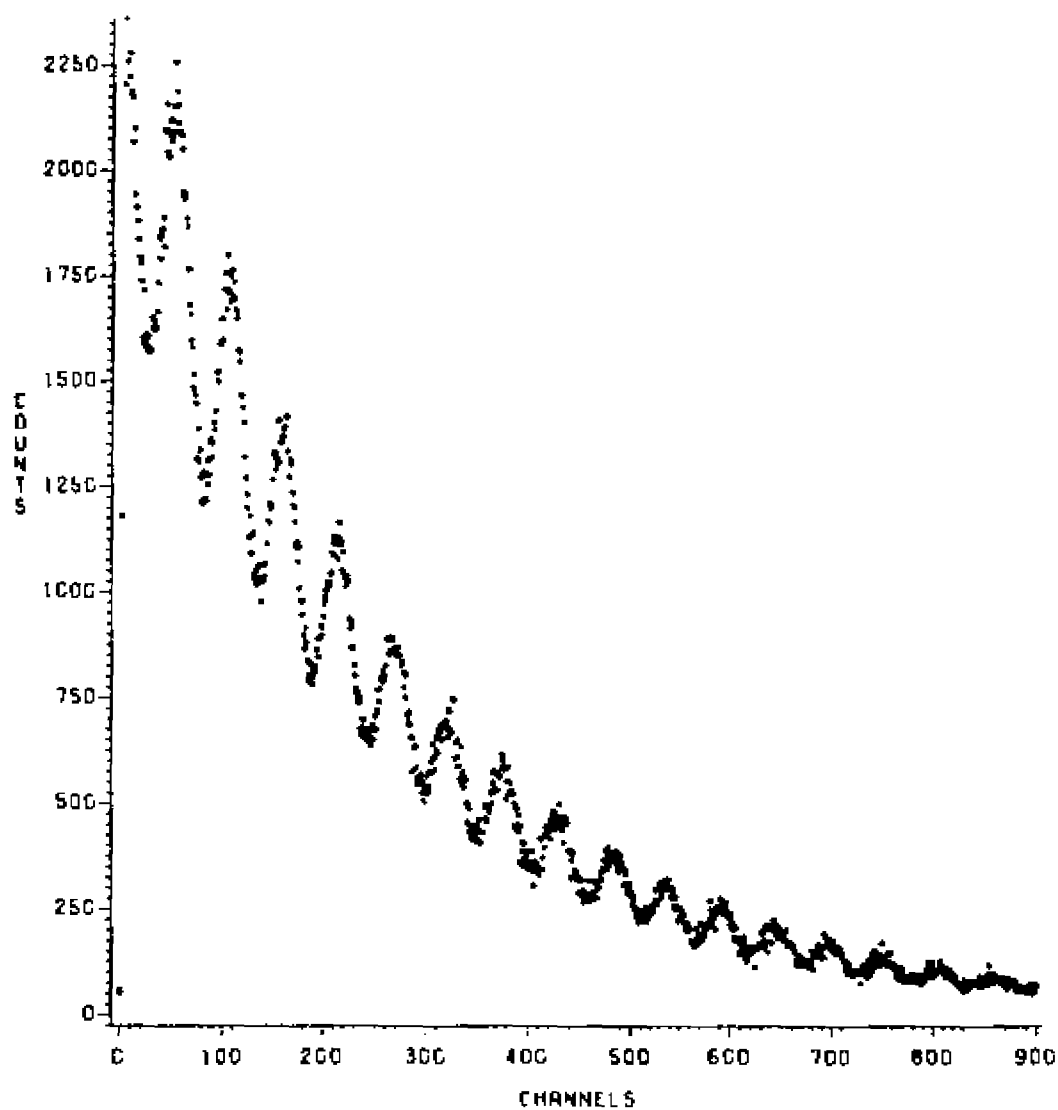


Figure 3.3b

A forward spectrum from BNL on AlMg at 295K, 150G. There are 117.9 channels per  $\mu\text{s}$ .  $a = 0.2$ ,  $\sigma = 0.064 \mu\text{s}^{-1}$ .

internal, bulk internal and terms from hyperfine interactions with electrons. The decay of polarization  $P_X(t)$ , depends on two factors. (1) The mean square dipole-dipole interaction with neighboring magnetic moments, represented by  $\Delta^2$ , the static second moment of random fields defined by,

$$\Delta^2/\gamma^2 = \langle H_X^2 \rangle = \langle H_Y^2 \rangle = \langle H_Z^2 \rangle \quad (3.11)$$

on which muon site determination depends.

(2) A correlation time  $\tau_C$ , describing the fluctuation of the random fields, which contains diffusion information.

Frequency can be determined by a least square fit to Eq. 3.10 or by a Fourier transform of the time histograms. For the depolarization often the following expression is used in Eq. 3.10,

$$P_X(t) = \text{EXP} (-\sigma^2 t^2) \quad (3.12)$$

and plots of  $\sigma(T)$ , the damping rate as a function of temperature are made. For a static muon  $\sigma^2 = \sigma_{VV}^2/2$ , due to motional narrowing of the random dipolar fields  $\sigma$  will become smaller as the muon moves. Therefore these plots provide qualitative information about muon diffusion. A more complete expression for the transverse relaxation function is:

$$P_X(t) = \text{EXP} [-\Delta^2 \tau_C^2 (e^{-t/\tau_C} - 1 + t/\tau_C)] \quad (3.13a)$$

$$= \text{EXP} (-\Delta^2 t^2/2) \quad \tau_C \rightarrow \infty \quad (3.13b)$$

$$= \text{EXP}(-\Delta^2 r_c t) \quad r_c \ll 1 \quad (3.13c)$$

What is  $\Delta^2 \gamma_{12}, 13$  The nuclear dipolar field at the origin from an i-th point dipole  $u_i$  located at  $r_i$  is given by,

$$H_i = (u_i/r_i^3) [3(\hat{u}_i \cdot \hat{r}_i)\hat{r}_i - \hat{u}_i] \quad (3.14)$$

with  $r$  taken to lie in the  $xz$ -plane ( $\phi$  set to 0), its  $z$  component can be expressed as (Fig. 3.4 and APPENDIX A):

$$H_{iz} = u_i/r_i^3 [(3 \cos^2 \theta_i - 1) \cos \phi_i + 3 \cos \theta_i \cos \phi_i \sin \theta_i \sin \phi_i] \quad (3.15)$$

In the transverse field case, where the following two conditions are satisfied:

- (1) The nuclear Larmor frequency  $\gamma_i H$  is larger than the width due to random fields  $\gamma H_i$ .
- (2) For the case of nuclear spin  $\geq 1$ , use of a large enough field so that the contributions of the electric field gradient created by the muon do not come into play.

The Larmor precession of  $u_i$  around  $H$  which is parallel to  $z$ , averages out the second term in Eq. 3.15 including  $\cos \phi_i$ . Therefore the second moment of the dipolar field components along  $H$  (Van Vleck Value) can be written as,

$$\sigma_{VV}^2 = 1/3 \gamma_\mu^2 \gamma_i^2 I(I+1) \hbar^2 \sum_i 1/r_i^6 (3 \cos^2 \theta_i - 1)^2 \quad (3.16)$$

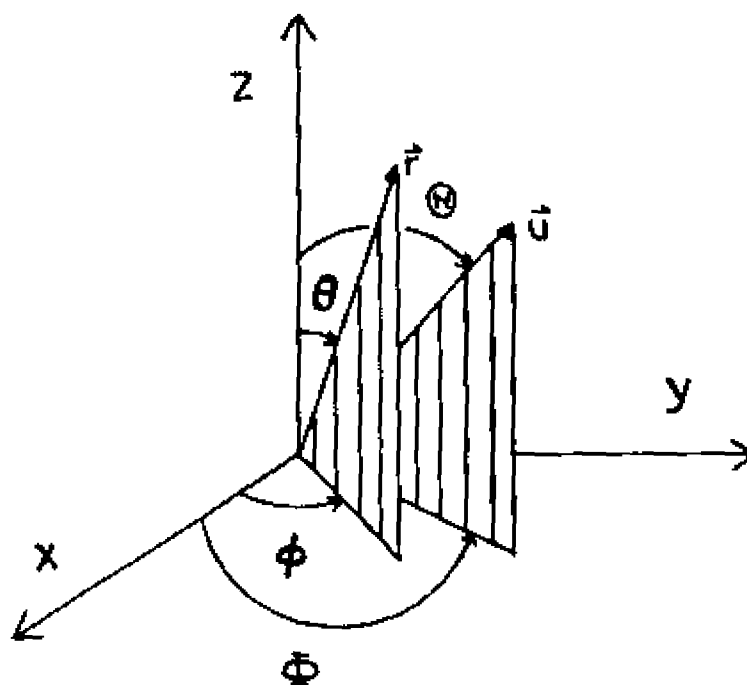


Figure 3.4

A representation of the angles in Eq. 3.15 which expresses the  $z$  component of the nuclear dipolar field at the origin, from an  $i$ -th point dipole  $u$  located at  $r$ .

where  $u_I = \gamma_I J \hbar$ ,  $J = I(I+1) \hbar$  and  $\langle \cos^2 \epsilon \rangle = (1/2) \int_0^\pi \cos^2 \epsilon \sin \epsilon \, d\epsilon$   
 $= 1/3$  has been used. Its polycrystalline average [  $\langle (3\cos^2 \theta - 1)^2 \rangle = 4/5$  ] is,

$$\sigma_{VV}^2 = 4/15 I(I+1) \gamma_I^2 \gamma_\mu^2 \hbar^2 \Sigma_1 r_I^{-6} \quad (3.17)$$

$\sigma_{VV}^2$  should be used in Eq. 3.13 a,b,c for  $\Delta^2$  if the two conditions stated above are satisfied.

#### F. Zero and Longitudinal Field $\mu$ SR

A pair of Helmholtz coils inserted with axis along the beam direction produce a magnetic field parallel to the beam and its polarization in the longitudinal case and no field for zero field studies. For either case Eq. 3.10 reduces to,

$$N_{F/A}(t) = N_{OF/A} \exp(-t/\tau_\mu) [1 + a_{F/A} P_z(t)] + \text{Bkgd.}_{F/A} \quad (3.18)$$

The time histogram (Fig. 3.5. zero field) does not have as much structure as in the case of transverse field data.

Data from the forward and backward detectors are combined in the following way to extract the experimental depolarization,

$$P_{z,\text{exp.}}(t) = [(N_F(t) - \text{Bkgd.}_F) - \alpha (N_A(t) - \text{Bkgd.}_A)] / [a_A(N_F(t) - \text{Bkgd.}_F) + \alpha a_F(N_A(t) - \text{Bkgd.}_A)] \quad (3.19)$$

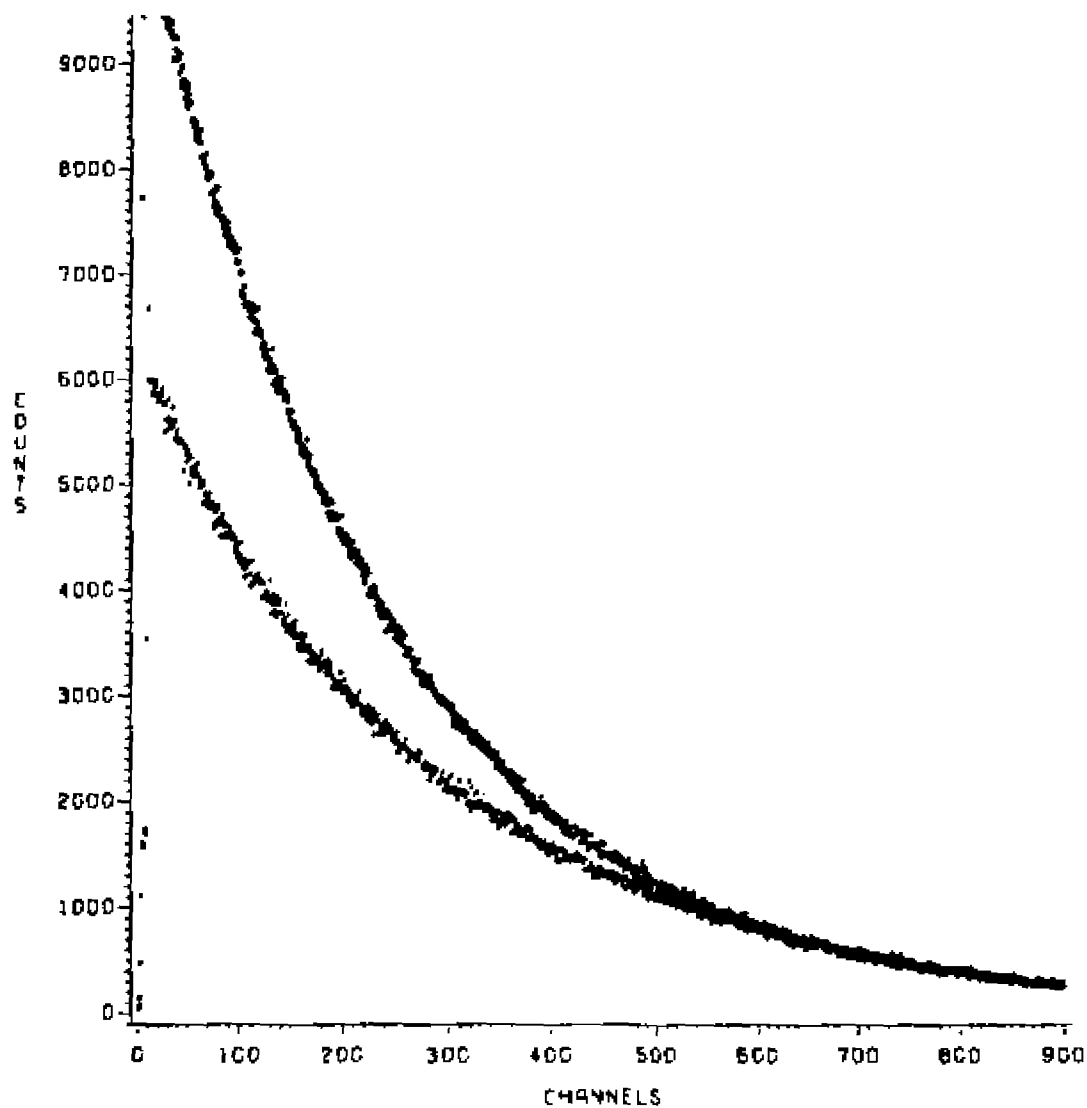


Figure 3.5  
Zero field data from BNL on AlMg at 10K. There are 117.9 channels per  $\mu$ s. The full stars are the forward spectrum while the open ones are the backward detected positrons.

where  $P_{z,exp.}(t)$  is the longitudinal relaxation function and  $a$  is the instrumental asymmetry =  $N_{OF}/N_{OA}$ .

The longitudinal relaxation can also be determined from each histogram independently by the following equation.

$$P_{z,exp.}(t) = [(N_F(t) - \text{Bkgd.}_F) \text{EXP}(t/\tau_\mu) - N_{OF}] / [(N_F(0) - \text{Bkgd.}_F) - N_{OF}] \quad (3.20)$$

The expression for the backward spectrum is similar to the above equation multiplied by a minus sign.

For longitudinal field  $\mu\text{SR}$  and for the case of static muon and random dipoles, the theoretical function used to fit  $P_{z,exp.}(t)$ , given by Eq. 3.19 or Eq. 3.20, is<sup>14</sup>:

$$P_{z,th.}(t) = 1 - 2 \Delta^2/\omega^2 [1 - \text{EXP}(-\Delta^2 t^2/2) \text{COS}\omega t] + 2 \Delta^4/\omega^3 \int_0^t \text{EXP}(-\Delta^2 r^2/2) \text{SIN}\omega r \, dr \quad (3.21a)$$

where  $\omega = \gamma_\mu B$

Its zero field limit is

$$P_{z,th.}(t) = 1/3 + 2/3 (1 - \Delta^2 t^2) \text{EXP}(-\Delta^2 t^2/2) \quad (3.21b)$$

The initial depolarization is Gaussian,

$$P_{z,th.}(t) = \text{EXP}(-\Delta^2 t^2) \quad (t\text{-short}) \quad (3.21c)$$

What is  $\Delta^2 \gamma^{12,13}$  At zero field the surrounding nuclei can precess due to quadrupole interactions produced by the positive muon. If this interaction is strong enough it can smear out the second term in Eq. 3.15. In this case the precession is along  $r_1$  and for random distribution of  $r_1$ , the average second moment is,

$$\Delta_{QI}^2 = 4/9 I(I+1) \gamma_I^2 \gamma_\mu^2 \hbar^2 \Sigma_1 r_1^{-6} \quad (3.22)$$

which is 5/3 times as large as the Van Vleck value. This value should be used in Eq. 3.21a,b as long as eqQ (section 3.1B) is strong.

In the case of no external field and no eqQ, as is the case for  $I=1/2$  nuclei at zero field, the second term in Eq. 3.15 does not drop out; then

$$\Delta^2 = 2/3 I(I+1) \gamma_I^2 \gamma_\mu^2 \hbar^2 \Sigma_1 r_1^{-6} \quad (3.23)$$

This value is 5/2 times as large as  $\sigma_{VV}^2$ , and should be used in Eq. 3.21a,b.

Compared to the transverse field second moment, the zero or longitudinal field moment is larger (Eqs.3.22 and 3.23), this results in faster depolarization. Also faster initial depolarization results from two components of the random fields contributing to the depolarization in zero or longitudinal field (Eq. 3.21c) compared to only one in the case of transverse field (Eq. 3.21b). Another useful characteristic

of zero and longitudinal field studies is the minima and recovery to  $1/3$  of the initial polarization for static muons (Eq. 3.21a,b).

The depolarization functions discussed so far are for static muons. Diffusion is sometimes described by a two state model<sup>14</sup>. In this model a muon diffuses and is captured by a trap in a mean time  $(1/\nu)$ ,  $\nu$  is the trapping rate, then released from traps after a mean time  $(1/\epsilon)$ ,  $\epsilon$  is the escape rate. The spin relaxation function can be expressed as an integral equation which can be solved numerically (APPENDIX B).

### 3.2 ELECTRONIC INTERACTION

The positive muons' electronic interaction with the metal ions is important in determining where they go in the lattice. Positive muons are repelled by nuclei located at lattice sites, therefore the potential minima are situated at interstitial points with Octahedral (O) or Tetrahedral (T) symmetry. In Face Centered Cubic (FCC) lattices the O sites form an FCC lattice with the same lattice constant  $a$  as the host. The interstitial lattice is displaced with respect to the host by  $a/2$  along the cube axis, and there is one O site per host atom (Fig. 3.6a). The T sites form a simple cubic lattice with constant  $a/2$  which is displaced by  $\sqrt{3} a/4$  along the cubic diagonal, and there are two T sites per host atom (Fig 3.6b). The interstitial sites in an FCC lattice have cubic symmetry. The situation is much more

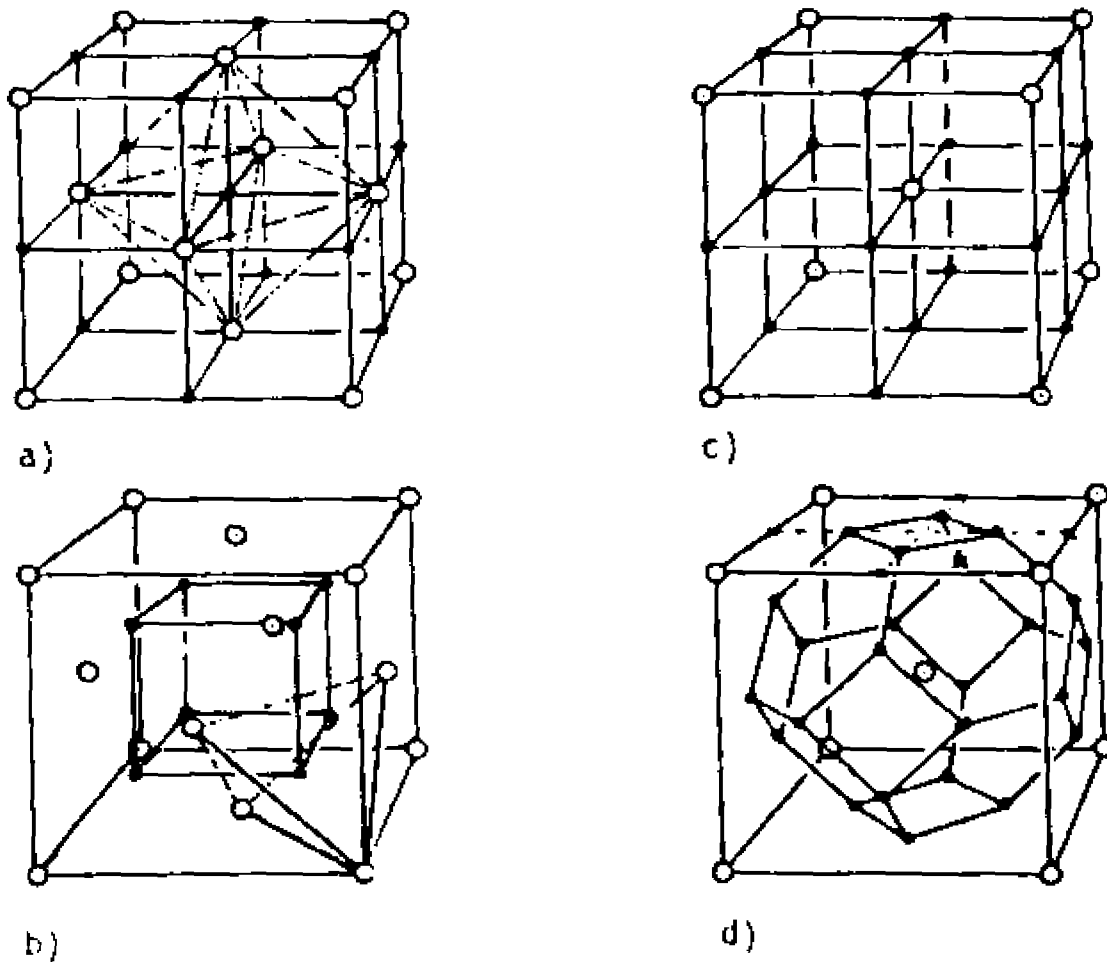


Figure 3.6a-d (K. Schroeder et al.)<sup>4</sup>  
 Various types of lattices of interstitial sites (full circles) in FCC and BCC lattices (open circles). The bold lines in a & b join the atoms forming one O and one T sites.

- (a) O sites in FCC form an FCC
- (b) T sites in FCC form a simple cubic lattice
- (c) O sites in BCC form three BCC lattices
- (d) T sites in BCC form six BCC lattices

complicated in Body Centered Cubic (BCC) lattices where there are three O sites and six T sites per host atom<sup>4</sup> as observed in Figs. 3.6c and d respectively. The interstitial sites in a BCC lattice have tetragonal symmetry.

Muons in metals are surrounded by conduction electrons so that, from a short distance the charged impurity appears neutral. For a free electron gas the mean radius of the screening cloud ( $r_s$ ) is related to the density  $n_{Ef}$  of the conduction electrons at the fermi level by<sup>3</sup>,

$$r_s = (E_f / 6\pi n_{Ef} e^2)^{1/2} \approx 1\text{\AA} \quad (3.24)$$

Self consistent electron density calculations around a proton in Al shows oscillations of the charge density within few Angstroms (Fig. 3.7). These oscillations should affect the interaction between a muon and an impurity in a crystal<sup>15</sup>.

Estreicher and Meier<sup>7</sup> have done pseudopotential calculations on the problem of muon trapping by substitutional impurities in metal. They predict strong trapping at the nearest and second nearest sites to the substitutional impurity in AlCu and AlAg, and weaker traps in AlMg and AlZn. The change in energy for sites further away is very small ( $\approx$  meV).

The conclusion to be drawn from the above is that the range of the electronic interaction is on the order of 4\AA or the nearest two sites to the impurity.

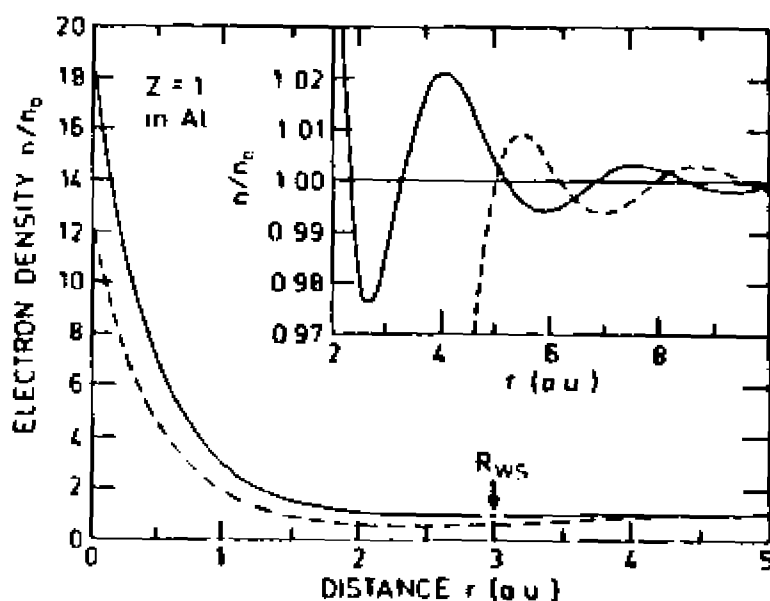


Figure 3.7 (M. Manninen et al.)<sup>15</sup>

Self consistent electron density around a proton in Al. The solid line is the density at interstitial sites and the dashed line is for substitutional sites.  $R_{ws}$  is the radius of the Wigner-Seitz cell which defines a region of space around a lattice point that is closest to that point than to any other lattice point. a.u. = 0.529 Å.

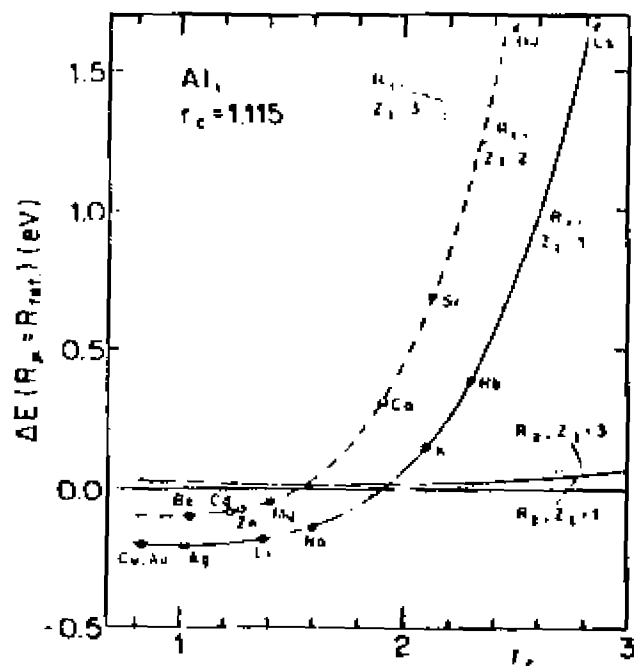


Figure 3.8 (S. Estreicher et al.)<sup>7</sup>

Change in the energy of a muon as a function of the core radius at nearest and second nearest T sites to a substitutional impurity with valence with respect to a T site in pure Al. The calculations were done using the Ashcroft empty-core pseudo-potential.

### 3.3 ELASTIC INTERACTION

#### A. Elastic Compliance and Stiffness Constants<sup>16</sup>

Strain is the measure of deformation. In strain analysis six coefficients are needed to define the strain. Neglecting terms of order  $\epsilon^2$ , the fractional change in the length of the axes are  $e_{xx}$ ,  $e_{yy}$  and  $e_{zz}$ , the other strain components  $e_{yz}$ ,  $e_{zx}$  and  $e_{xy}$  are defined in terms of the change in angle between the axes. The force acting on a unit area in a solid is defined as the stress. With the condition that the angular acceleration vanish, and hence the total torque be zero, six independent stress components  $X_x$ ,  $Y_y$ ,  $Z_z$ ,  $Y_z$ ,  $Z_x$  and  $X_y$  describe the stress. The capital letter indicates the direction of the force and the subscript indicates the normal to the plane to which the force is applied. Hooke's law states that for small deformation the strain is directly proportional to the stress,

$$e_{xx} = S_{11}X_x + S_{12}Y_y + S_{13}Z_z + S_{14}Y_z + S_{15}Z_x + S_{16}X_y \quad (3.25a)$$

$$e_{yy} = S_{21}X_x + S_{22}Y_y + S_{23}Z_z + S_{24}Y_z + S_{25}Z_x + S_{26}X_y \quad (3.25b)$$

or

$$X_x = C_{11}e_{xx} + C_{12}e_{yy} + C_{13}e_{zz} + C_{14}e_{yz} + C_{15}e_{zx} + C_{16}e_{xy} \quad (3.26c)$$

Similar expressions exist for the other components.

The S's are the elastic compliance constants.

The C's are the elastic stiffness constants.

In a cubic crystal there are only three independent stiffness constants.

	$e_{xx}$	$e_{yy}$	$e_{zz}$	$e_{yz}$	$e_{zx}$	$e_{xy}$
$X_x$	$C_{11}$	$C_{12}$	$C_{12}$	0	0	0
$Y_y$	$C_{12}$	$C_{11}$	$C_{12}$	0	0	0
$Z_z$	$C_{12}$	$C_{12}$	$C_{11}$	0	0	0
$Y_z$	0	0	0	$C_{44}$	0	0
$Z_x$	0	0	0	0	$C_{44}$	0
$X_y$	0	0	0	0	0	$C_{44}$

#### B. Distortions Around a Point Defect

The distortion produced by a positive muon in the surrounding lattice is important in determining its state in a pure crystal, in the presence of other point defects as in the Al(Impurity) experiment of chapter 4, or when a uniaxial stress field is applied as in the iron experiment of chapter 5. Therefore a model to describe the displacement of atoms from their regular sites by a point defect is needed. These displacements can be thought of to result from the fictitious Kanzaki forces<sup>6</sup> in a defect free lattice (Fig. 3.9). In the framework of continuum theory, force densities can be used, which must have vanishing total force and torque (equilibrium conditions). Therefore the double force tensor defined by Eq. 3.26 is the first nonvanishing term in the multipole expansion of the displacement field, and is sufficient to characterize the macroscopic situation.

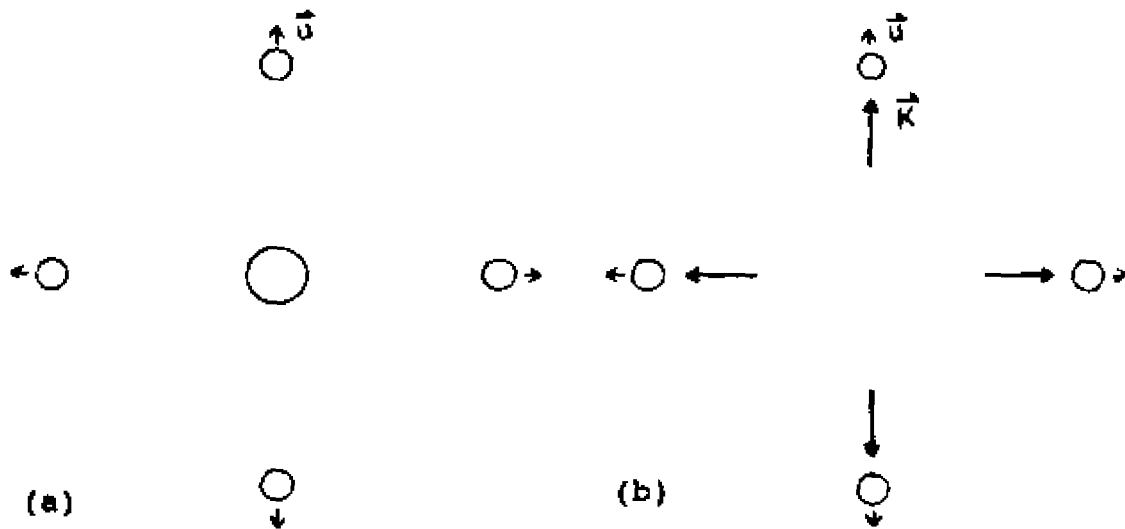
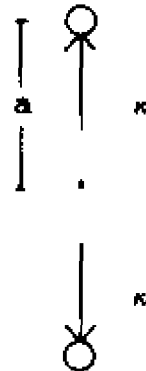


**Figure 3.9**  
 The Kanzaki forces. In (a)  $u$  is the displacement of atoms due to the impurity atom. In (b) the impurity atom is replaced by a regular atom and  $u$  results from the Kanzaki force  $\kappa$ . In continuum theory  $u$  and  $\kappa$  are the displacement and force fields.

$$P_{ij}(i,j = x,y,z) = \int dr x_i f_j(r) \quad (3.26)$$

The double force tensor can be described with the following picture.<sup>6</sup>



The force density  $f_z(r) = \kappa[\delta(z-a) - \delta(z+a)] \delta(x) \delta(y)$

From equation 3.26 the double force tensor is,

$$P_{ij} = 2\kappa a \begin{vmatrix} 0 & 0 & 0 \\ 0 & 0 & 0 \\ 0 & 0 & 1 \end{vmatrix}$$

For a center of dilation in a cubic crystal the double force tensor per unit volume per unit defect is,

$$P_{ij}/V = \begin{vmatrix} X_x & 0 & 0 \\ 0 & Y_y & 0 \\ 0 & 0 & Z_z \end{vmatrix}$$

where  $X_x, Y_y$  and  $Z_z$  are the stress components.

Another way to characterize a defect and its distortion field in a crystal is by elastic dipoles. A  $\lambda$ -tensor<sup>17,18</sup>, which represents the strain per unit volume per unit defect.

$$\lambda_{ij} = \begin{vmatrix} e_{xx} & 0 & 0 \\ 0 & e_{yy} & 0 \\ 0 & 0 & e_{zz} \end{vmatrix}$$

The change in volume per unit volume associated with a defect is to first order,

$$\Delta V/V = \text{Tr. } \lambda_{ij} = \text{Tr. } P_{ij} / [V(C_{11}+2C_{12})] \quad (3.27)$$

The change in volume can be measured as a change in the lattice parameter,

$$\begin{aligned} \Delta a/a &= 1/3 \Delta V/V = 1/3 n/N \Delta V_I/\Omega \\ \Delta V_I/\Omega &= 3/a da/dc \end{aligned} \quad (3.28)$$

Where  $V$  is the volume,  $n$  is the number of point defects,  $\Delta V_I$  the change in volume per defect,  $N$  number of lattice atoms,  $\Omega$  the volume per atom and  $da/dc$  is the contraction or expansion of the lattice constant with increased solute concentration (Fig. 4.3). For an isotropic elastic continuum (FCC)  $P$  can be expressed as,

$$P = (C_{11}+2C_{12}) \Omega/a da/dc \quad (3.29)$$

### C. Interaction Between Two Point Defects

An interstitial muon in a crystal displaces the surrounding atoms and could create a deep potential well for self trapping. The trapping site will be one with O or T symmetry, because of the relatively large available space and hence least deformation and the electrostatic repulsion by atoms on lattice sites. If self trapping is delayed, impurities can induce trapping.

The interaction energy of two point defects in general cannot be given in a closed form due to the complicated structure of the lattice Green's function. For a qualitative analysis of the  $\mu$ SR data on Al(Impurity) systems discussed in chapter 4 use is made of the following two results:

(1) The long range interaction energy is given by the results of continuum theory<sup>4</sup>, it goes as,

$$E(R) = - (\text{Const.}/R^3) f(\Omega) \quad (3.30)$$

Its main features are:

- a- Falls off with distance as  $R^{-3}$ , similar to the interaction between two magnetic dipoles.
- b- The interaction averaged over the solid angle is zero,  $\int d\Omega f(\Omega) = 0$ , this implies that there are always attractive and repulsive directions irrespective of the local deformation caused by the point defect.
- c- For FCC crystals, to lowest order in the anisotropy parameter  $d = C_{11} - C_{12} - 2C_{44}$  and for isotropic defects,

$$E(R) = -15d/8 \times [5/(3C_{11} + 2C_{12} + 4C_{44})]^2 P^A P^B / R^3 \times (3/5 - \epsilon_1 R_1^4 / R^4) \quad (3.31)$$

where A and B are the two point defects. For most metals  $d < 0$ , and for identical defects ( $P > 0$ ) the interaction is attractive in the  $\langle 100 \rangle$ - and  $\langle 110 \rangle$ - directions and repulsive in the  $\langle 111 \rangle$ - directions.

2) Atomic displacements close to the impurity can be large, changing the coupling between atoms. The hydrogen-substitutional impurity interaction energies in BCC metals (Nb, V, Ta) have been calculated using the theory of lattice statics by Shirley and Hall<sup>5</sup>. Their results show that the interaction for sites other than the nearest and second nearest neighbor to be sensitive to distance and orientation in agreement with the results of continuum theory summarized above. While for the closest two sites the interaction depends on  $da/dc$  of the substitutional impurity. If  $da/dc > 0$  ( $P > 0$ ) then the interaction will be attractive, but if  $da/dc < 0$  ( $P < 0$ ) it will be repulsive.

#### D. Muon-Uniaxial Stress Interaction

A point defect (muon) can be described as an elastic dipole (section 3.3B). In a similar way to the alignment of a magnetic dipole in an external magnetic field, the elastic dipole should align in an external stress field. In chapter 5 this is shown to be the case for a muon in iron under uniaxial stress. In this section we split the muon energy

between structurally equivalent sites due to uniaxial stress is derived.

In a BCC lattice the interstitial sites have tetragonal symmetry. The  $\lambda_{ij}$  for  $O_1$  and  $O_2$  or  $T_1$  and  $T_2$  (chapter 5, Fig. 5.1a,b) can be written in the following form ( $e_d > e$ ),

$$\lambda_{ij}(O_1) = \begin{vmatrix} e_d & 0 & 0 \\ 0 & e & 0 \\ 0 & 0 & e \end{vmatrix}, \text{ or } \lambda_{ij}(O_1) = \begin{vmatrix} e & 0 & 0 \\ 0 & e_d & 0 \\ 0 & 0 & e \end{vmatrix}$$

$$\lambda_{ij}(O_2) = \begin{vmatrix} e & 0 & 0 \\ 0 & e & 0 \\ 0 & 0 & e_d \end{vmatrix}$$

With the uniaxial stress along the z axes, the energy difference for muons between sites  $O_1$  and  $O_2$  ( $T_1$  and  $T_2$ ) can be written in analogy to magnetic dipoles in a magnetic field. Therefore,

$$\Delta E = E_{O1} - E_{O2} = -\sigma_{zz} [\lambda_{33}(O_1) - \lambda_{33}(O_2)] = (e_d - e) \sigma_{zz}$$

For a muon in a site with tetragonal symmetry the double force tensor has the following form,

$$P_{ij} = \begin{vmatrix} P_d & 0 & 0 \\ 0 & P & 0 \\ 0 & 0 & P \end{vmatrix}; \text{ Then } \begin{aligned} e_d &= S_{11}P_d + 2S_{12}P \\ e &= S_{11}P + S_{12}P + S_{12}P_d \end{aligned}$$

$$\text{Therefore: } \Delta E = ((S_{11} - S_{12})/S_{11}) (P_d - P) e_{001} \quad (3.32)$$

## E. Conclusion

In the above section a muon was represented as an elastic dipole. Its interaction with other point defects (elastic dipoles) or uniaxial stress field was investigated along the lines of the interaction of two magnetic dipoles or that of a dipole and a magnetic field. In the next two chapters these interactions will be studied by two experiments. Chapter 4 will describe the Al(Impurity) experiment where the elastic dipole-dipole interaction was used to give a qualitative explanation of the data. Chapter 5 will describe the uniaxial stress experiment on iron where the elastic dipole-uniaxial stress interaction will be used to explain the observed strain induced muon frequency shift.

## Chapter IV

### DIFFUSION AND TRAPPING IN Al(IMPURITY) ALLOYS

#### 4.1 OVERVIEW

The damping of the  $\mu$ SR signal in a pure host (Eq. 3.12), is expected to change from a small value corresponding to the motional narrowing of the random dipolar fields at high temperature toward a larger value determined by the static fields at lower temperatures (Fig. 4.1). A muon is considered static if it does not move during the time of observation which is on the order of  $10^{-5}$  s.

Magnetic metals with large dipole fields from unpaired electrons (section 3.1A) can be used to study fast jump processes. For non-magnetic metals to be suitable for  $\mu$ SR studies their nuclear moments should be large enough to give a reasonable depolarization in a 10  $\mu$ s time window. BCC Nb and V, and FCC Cu and Al are the non-magnetic metals most studied by  $\mu$ SR<sup>3,14</sup>. Diffusion in relatively pure copper ( < 20 ppm interstitials, < 1 ppm substitutional impurities ) reveals for  $\rho(T)$  the general shape in Fig.4.1, with some deviations on the low temperature side. Since for moderately pure Al the damping rate is low over all temperatures, Al is ideal to study impurity effects.

Al(Cu), Al(Mg), Al(Ag), Al(Mn) and Al(Zn) are some of the Al(Impurity) systems studied by transverse field over a wide

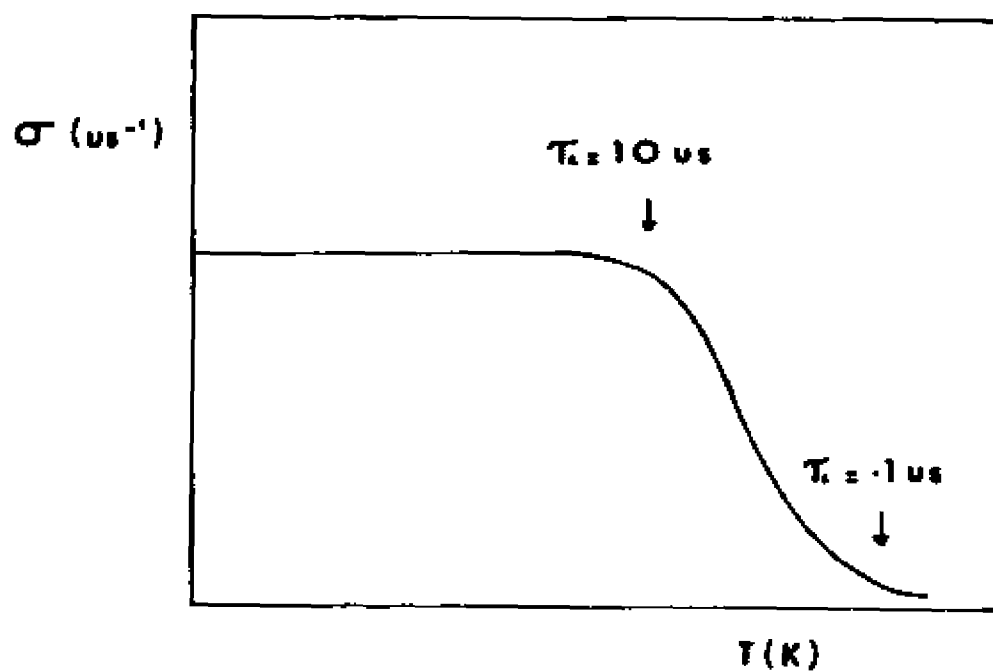


Figure 4.1

Expected behavior of the damping parameter of the  $\mu\text{SR}$  signal for metal as a function of temperature.  $\tau_c$  is a correlation time describing the fluctuation of the random fields.

TABLE 4.1  
Aluminum (Al) data

Crystal structure	FCC	Valence	+3
Lattice constant	4.05 Å	$C_{11}$	0.73eV/Å <sup>3</sup>
Spin	5/2 $\mu_B$	$C_{12}$	0.40eV/Å <sup>3</sup>
Magnetic moment	3.64 $\mu_N$	$C_{44}$	0.19eV/Å <sup>3</sup>

range of temperature<sup>19,20,21</sup>. It was found that the damping rate is a complicated function of temperature which results from trapping (Fig. 4.2a,b,c,d,e). The first part of this chapter deals with muon diffusion in AlCu<sub>420ppm</sub>, using the zero and low longitudinal field technique, analyzing the data on the basis of the trapping-detrapping model (section 3.1F, APPENDIX B)<sup>14</sup>. The second part looks at transverse, zero and longitudinal field experiments on AlMg and AlAg alloys. The aim is for a better understanding of the diffusion and trapping mechanisms and how they are related to the strain fields in these systems.

The zero and low longitudinal field experiments are complementary to the transverse field method in the study of diffusion and trapping. Compared to the transverse field they have 1)Faster depolarization, as seen in section 3.1F, this is the result of two components of the random field each

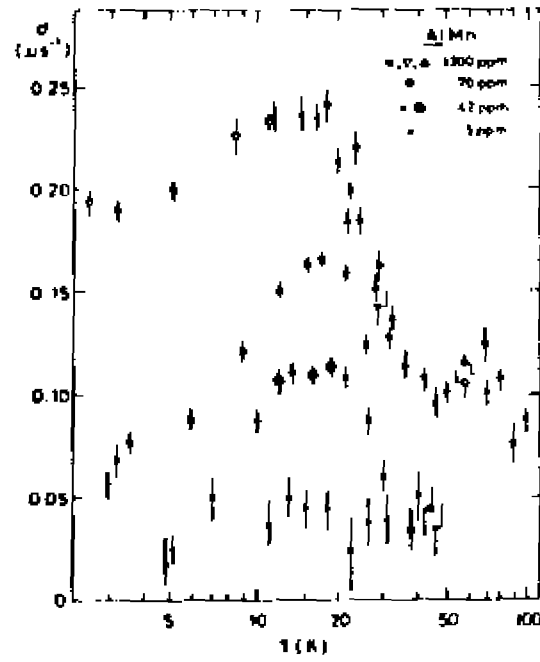


Figure 4.2a (K.W.Kehr et al.)<sup>21</sup>  
Damping parameter for AlMn alloys.

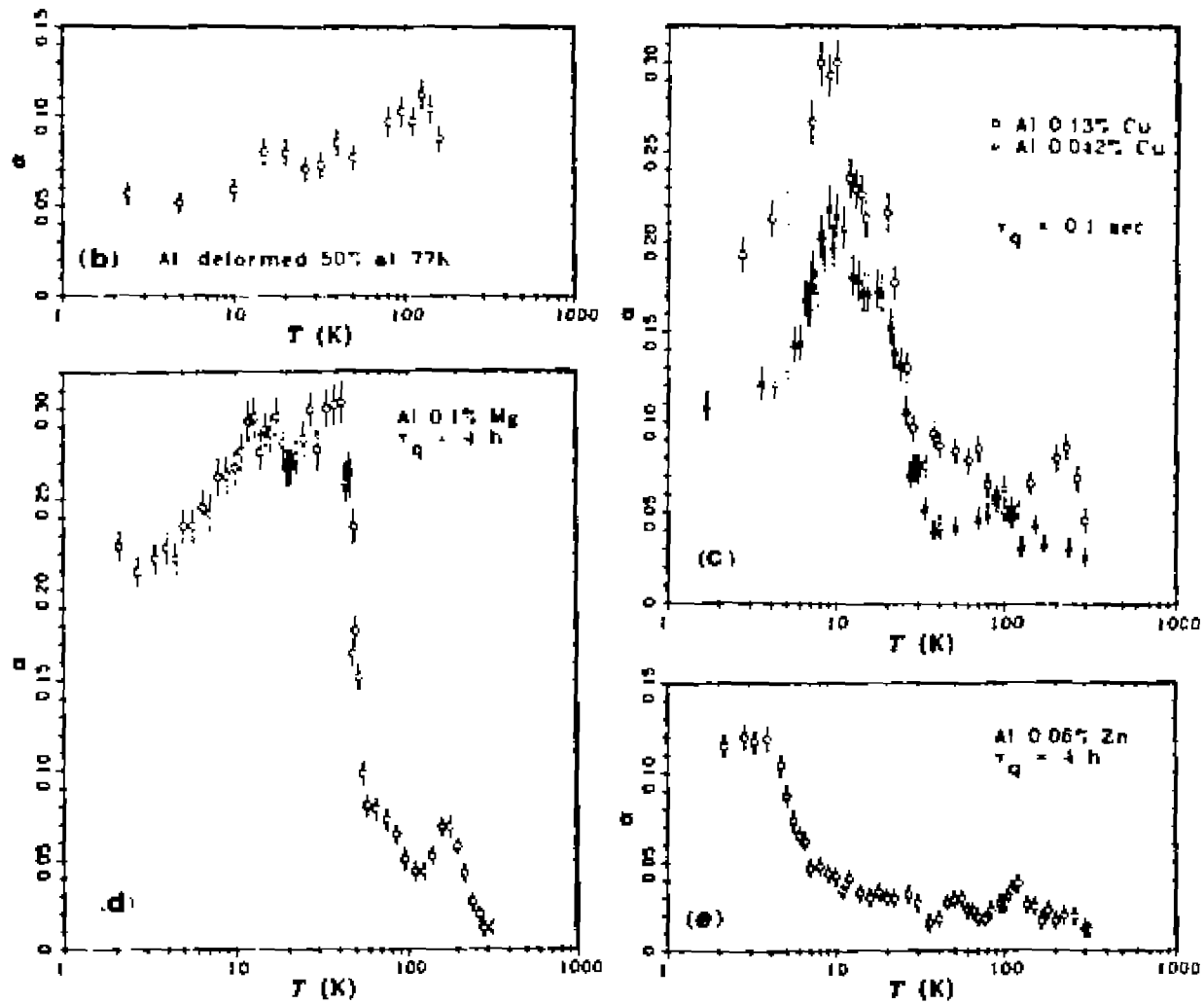


Figure 4.2b-e (W.J.Kossler et al.)<sup>20</sup>  
 Damping of the  $\mu$ SR signal versus temperature at a field of 500 G  
 where  $\sigma = 2 \sigma^2 \tau_{\mu}^2$ .

represented by the zero field second moment contributing to depolarization, compared to only one component represented by the smaller transverse second moment. 2) The minima at  $t = \sqrt{3} / \Delta_Z$  and recovery to 1/3 is the sign of a static field environment ( 1/3 of the random fields are in the direction of the muon spin at time zero, Eq. 3.21b, Fig. 4.8). To see the minima and recovery it should be possible to look at a time, depending on the size of the random fields, of 8 to 14  $\mu$ s. Due to the exponential decay few muons live long enough to give counts after 10  $\mu$ s. Therefore it is essential for the data spectra in this kind of experiment to have many events and a well determined low background.

#### 4.2 SYMMETRY BREAKING

To understand muon diffusion and trapping in Al-impurity systems the electronic and elastic perturbation in the Al lattice due to the point defects (impurities and muon) must be considered. Lattice dilation in Al due to substitutional impurities can be obtained from Eq. 3.28, using the change in lattice parameter reported by Pearson<sup>22</sup>(table 4.2 & Fig.4.3).

In a crystal with impurities, the possible sites for a muon are no longer equivalent; there are energy differences between neighboring sites. Close to the impurity ( $< 4A$ ), both the electronic (section 3.2) and elastic (section 3.3C) interactions have to be considered. Farther out, due to screening of the charge impurity by valence electrons, only the elastic part contributes to muon trapping. In this region

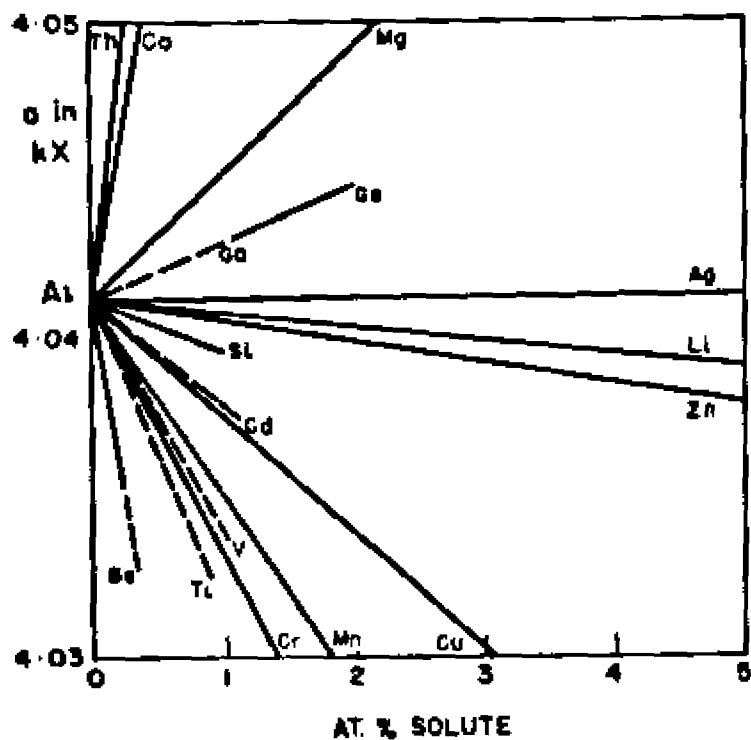


Figure 4.3 (Pearson et al.)<sup>22</sup>  
 Lattice spacings of Al solid solutions as a function of  
 composition ( $1.00202 \text{ kX} = 1 \text{ \AA}$ )

TABLE 4.2

Lattice dilation in  $Al^{3+}$  due to substitutional (Sub.) and interstitial (Int.) impurities, also listed are the impurities spin and magnetic moment.

Sub.	Spin ( $\uparrow$ )	$u(u_N)$	$\Delta a/a$ for 1 atomic %	$\Delta V(A^3)$
$Mg^{2+}$	0	0	$+0.93 \times 10^{-3}$	+4.6
$Cu^{1+}$	3/2	2.28	$-1.3 \times 10^{-3}$	-6.5
$Ag^{1+}$	1/2	-0.12	$< 10^{-5}$	$< 0.05$
$Zn^{2+}$	0	0	$-0.13 \times 10^{-3}$	-0.6
$Mn^{2+}$	5/2	3.44	$-1.5 \times 10^{-3}$	-7.4
Int. (reference 21)				
$H^{1+}$	1/2	2.79		+2.9

impurities that expand or contract the lattice will have attractive sites (section 3.3C). The escape rate is described by the Arrhenius law ( $E_a$  is the activation energy).

$$1/\tau_c = 1/\tau_0 \text{ EXP}(-E_a/kT) \quad (4.1)$$

Beyond the trapping region there are energy differences between interstitial sites due to the long range strain fields. An estimate of the energy difference  $\Delta E$  in the region far from the defect can be obtained from Eq. 3.31. For the estimate  $(3/5 - \sum_j (R_j/R)^4) \approx 0.5$ ,  $d = 0.05 \text{ eV}/A^3$ ,

$[5/(3C_{11}+2C_{12}+4C_{44})]^{-2} = 1.8 \text{ (Å}^3/\text{eV)}^2$ ,  $P^{\text{Cu}} = 3.3 \text{ eV}$  and  $P^{\mu} = 1.5 \text{ eV}$  (Eq. 3.29, table 4.1 and table 4.2). One finds  $E(R) = 0.13/R^3 \text{ eV}$  ( $R$  in Å). For 500 ppm Cu in Al,  $R$  taken midway between two point defects  $\approx 16\text{Å}$ .  $E(16\text{Å})$  due to one point defect is  $\approx 30 \mu\text{eV}$ , therefore the energy difference  $\Delta E$  between neighboring interstitial sites ( $\Delta R \approx 2\text{Å}$ ) is a few  $\mu\text{eV}$ . When  $kT$  (at 10 K  $\approx 860 \mu\text{eV}$ )  $\gg \Delta E$ , the absorption or emission of a single phonon can result in a transition between sites of the same symmetries ( $O \rightarrow O$  or  $T \rightarrow T$ ). The transition rate is given by (K.W.Kehr et al.)<sup>21</sup>,

$$\Gamma_{\text{abs.}} = \Gamma_{\text{em.}} = [(J_{\text{eff.}} P \Delta E \Delta R)^2 / (12 \pi \rho \hbar^6 c^7)] kT \quad (4.2)$$

where  $J_{\text{eff.}}$  is the effective transfer matrix element,  $\rho$  is density of host metal and  $c$  is the velocity of sound. If the energy difference between a muon in an O-site and T-site is  $\Delta E_{\text{OT}}$ , the one phonon transition rate between sites of different symmetries ( $O \rightarrow T$  or  $T \rightarrow O$ ) in the high temperature approximation is<sup>21</sup>,

$$\Gamma = (J_{\text{eff.}}^2 [\text{Tr.}(P_j) - \text{Tr.}(P_i)]^2 / 2\pi \rho \hbar^4 c^5) kT \quad (4.3)$$

plus a term equivalent to Eq. 4.2. It is important to note that both terms of the one phonon process are linear in temperature. All other phonon processes have a more complicated temperature dependence (K.W.Kehr et al.)<sup>21</sup>.

### 4.3 EXPERIMENTS, RESULTS and INTERPRETATIONS

#### A. Fitting

A least square fitting fortran routine that uses an algorithm which combines the best of the gradient search with the method of linearizing the fitting function was used (Marquardt)<sup>23</sup>.

#### B. Samples

The aluminum impurity alloys used are described by Kossler et al.<sup>20</sup>. Transverse field data on these samples are shown in Fig. 4.2c,d. Where  $\sigma = 2 \sigma^2 r_{11}^2$ .

#### C. AlCu<sub>420</sub>ppm

Experiment: Four 3mm thick sample plates were stacked inside a He flow cryostat, the temperature was measured with a carbon resistor and controlled to 0.1K. The field was nulled to 0.1G. Typical stopping muon rates were 2000 s<sup>-1</sup>, with event rates of 300 s<sup>-1</sup>. Data was taken for about an hour per point corresponding to one million events.

Analysis and results: The experimental depolarization was extracted from the forward and backward positron spectra according to Eq. 3.19. A transverse field run at 7.1K and 150G was used to find the background ratios (Bak.F/N<sub>0F</sub> and Bak.A/N<sub>0A</sub>) and normalization parameter  $\sigma$ , which were then fixed for all zero field runs. Also extracted from the

transverse data and fixed for all runs were the asymmetries ( $a_F$  and  $a_A$ ).  $N_{OF}$  and  $N_{OA}$  needed to calculate the backgrounds were found from fitting the data directly to Eq. 3.18. The cryostat was moved just before the 14.2G runs. In order to determine the above parameters for these runs,  $\alpha$  from fitting directly to Eq. 3.18 was scaled according to the difference in  $\alpha$  between zero field data and the transverse run. Then the background ratios were adjusted in a manner to be consistent with the change in  $\alpha$ . The new set of ( $\alpha$ ,  $Bkgd.F/N_{OF}$ ,  $Bkgd.A/N_{OA}$ ) was then held constant for all the 14.2G runs.

The zero and longitudinal field spin relaxation spectra  $P_{z,ext.}(t)$ , were fitted to the calculated  $P_{th.}(t)$  (APPENDIX B<sup>14</sup>) considering one kind of traps with second moment  $\Delta_z$ , trapping rate  $\nu$  and escape rate  $\epsilon$ . In order to reduce the uncertainty in  $\nu$ ,  $\Delta_z$  was fixed to the values obtained in the previous step and the data refitted with  $\nu$  and  $\epsilon$  as free parameters; the results are shown in table 4.3.

All the runs at 20K and 22K were fitted with  $\Delta_z$  fixed to  $0.38 \mu s^{-1}$  which was found to increase  $\chi^2$  by about 20%. Fig. 4.4 shows the data and fit with the parameters given in table 4.3. In Fig. 4.5 the trapping  $\nu$  and escape  $\epsilon$  rates are plotted as a function of temperature.

Interpretation: Even though the maximum in the trapping rate is at 14K (Fig. 4.5), due to the lower escape rate muons actually spend more time in traps at 10K. This is in agreement with the peak in the damping rate Fig. 4.2c.

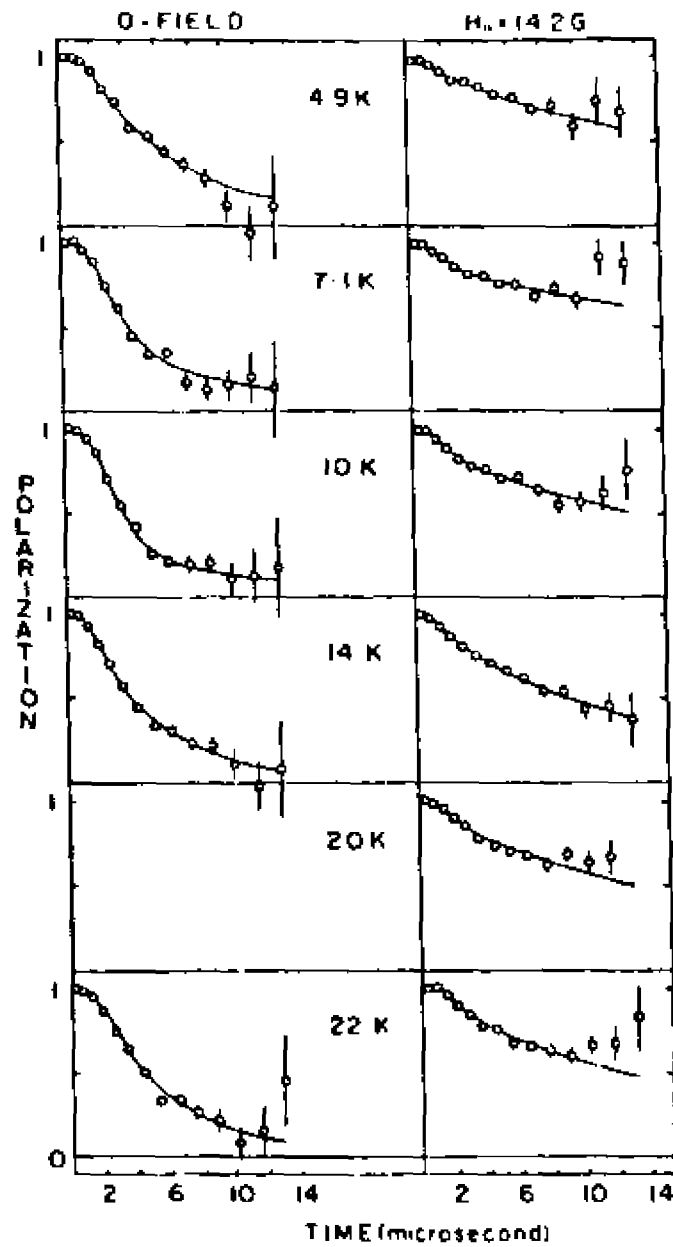


Figure 4.4  
 Muon polarization as a function of time in AlCu<sub>420</sub>ppm. The parameters of the fitting function are given in table 4.3.

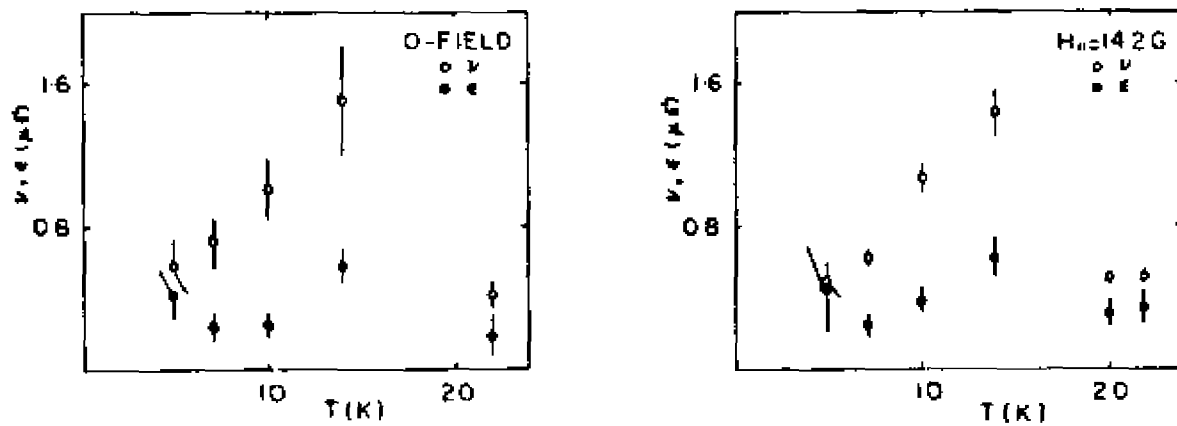


Figure 4.5  
The trapping  $\nu$  and escape  $\epsilon$  rates as a function of temperature for AlCu.

TABLE 4.3

Results of zero and 14.2G experiment on AlCu<sub>420ppm</sub>  
 Fit to the two-state model (APPENDIX B)<sup>14</sup>,  $\nu$  is the trapping  
 rate and  $\epsilon$  is the escape rate

T(K)	$\Delta_Z (\mu\text{B}^{-1})$	0-field		14.2G longitudinal	
		$\nu (\mu\text{B}^{-1})$	$\epsilon (\mu\text{B}^{-1})$	$\nu (\mu\text{B}^{-1})$	$\epsilon (\mu\text{B}^{-1})$
4.9	0.38	0.58±0.15	0.42±0.14	0.49±0.09	0.45±0.24
7.1	0.38	0.72±0.13	0.24±0.08	0.62±0.05	0.25±0.06
10	0.38	1.01±0.18	0.25±0.07	1.07±0.08	0.39±0.07
14	0.41	1.50±0.31	0.59±0.10	1.43±0.13	0.63±0.11
20	0.47			0.52±0.03	0.32±0.08
22	0.47	0.42±0.08	0.19±0.12	0.52±0.04	0.35±0.09

For a constant concentration of traps in a crystal, the faster a muon moves the sooner it will find a trap. Therefore, the trapping rate up to the peak should be proportional to the transition rate, which is linearly proportional to temperature for the one phonon processes (Eq. 4.2 or Eq. 4.3). A least square fit of  $\nu = T^\beta$  to the trapping rates between 4.9K and 14K for the 0-field and 14.2G data listed in table 3.3, gives a  $\beta$  of  $0.93 \pm 0.26$  and  $1.16 \pm 0.14$  respectively. On the basis of the above result the hopping of muons between different sites seems to be induced by a single phonon. Kehr et al.<sup>21</sup> did not observe any dependence of the muon hopping rate on  $\Delta E$  in the case of Mn impurity in

TABLE 4.4  
 $\Delta Z(QI)$  ( $\mu s^{-1}$ ) calculated from Eq. 3.22

---



---

	lattice sums <sup>24</sup>	nearest neighbors N.N.	relaxation N.N. $\Delta R/R = 10\%$
T	0.484	0.475	0.36
O	0.387	0.378	0.28
V	0.203		

---

Al and as a result predict a transition between crystallographically inequivalent sites (Eq. 4.2 and Eq. 4.3) , [ $\Delta E \ll \Delta E_{OT} \ll kT$ ]. Therefore the one phonon diffusion process does not result from the long range strain fields associated with impurities but from the difference in energy between O and T sites for muons in a pure crystal.

To compare the possible muon trapping sites,  $\Delta Z$  for a strong quadrupole interaction calculated from Eq. 3.22, for tetrahedral- octahedral- and vacancy- sites in a rigid Al lattice are listed in table 4.4.

Comparing the  $\Delta Z$  in table 4.3 and those in table 4.4 we consider two possibilities for the trapping site. In the first case muons trap in a T-site with 10% relaxation of N.N. ions. The macroscopic volume change can be calculated as (section 3.3B, Eq. 3.28 and Eq. 3.29)  $\Delta V = \frac{1}{3} K a$

$/(C_{11}+2C_{12})$ . For a central force, the force constant along the  $\langle 100 \rangle$  direction on N.N. in an FCC lattice is  $\alpha_1 = C_{44}a^{25}$ . For a T-site with 10% relaxation the  $\mu^+$ -Al force is  $K = 6 a C_{44} \cos^2(35.3) \delta R = 0.53 \text{ eV/\AA}$ . Therefore  $\Delta V = 2.4 \text{ \AA}^3$ , in agreement with the hydrogen result listed in table 4.2. The deeper traps at higher temperatures are possibly closer to the defect (14K the start of mixed traps), where lattice contractions due to Cu offset the relaxation caused by muons, leading to larger  $\Delta_2$ . The second possibility is that the preferred site changes from O-site to T-sites as the temperature is raised where in both cases there is no lattice relaxation. This model does not agree with the results of hydrogen and predicts a pure electrostatic trapping in contradiction to the strong trapping peak seen next in AlMg.

The change in the value of  $\Delta_2$  (table 4.3) implies a change in the muon trapping site. This change is possible if an extended trapping region that contains many trapping sites exists around a point defect. The idea of extended trapping regions around impurities was introduced in section 4.2.

#### D. AlMg<sub>1000</sub>ppm

Experiment: Three 3mm plates were placed in a closed-cycle He refrigerator (Displex), the temperature between 10K and 50K was measured with a thermocouple to which a correction ( $< 3\text{K}$ ) was applied because of the position of the thermocouple relative to the sample. Higher temperatures were measured with a platinum resistor placed on the cold

Table 4.5

Transverse field results on  $\text{AlMg}_{1000\text{ppm}}$ ;  $\Delta\chi$  and  $\tau_C$  are the average values on the plateau and  $E_a$  is for the drop off.

Region	T(K)	$\Delta\chi(\mu\text{s}^{-1})$	$\tau_C(\mu\text{s})$	$E_a(\text{meV})$
I	10 --- 60	$.317 \pm .007$	4 --- 10	$20 \pm 1$
II	60 --- 150	$.221 \pm .013$	1 --- 2	$29 \pm 5$
III	150 --- 300	$.150 \pm .013$	6 --- 10	$95 \pm 34$

finger. The muon stopping rate was  $5000 \text{ s}^{-1}$ , which gave a count rate of 600 events/s. Transverse field runs were taken for half an hour corresponding to one million events, longitudinal runs for one hour or two million events and zero field for two hours or four million events.

Analysis and results: The transverse field runs were done at 150G. Fig. 4.6 shows the damping parameter (Eq. 3.12) versus temperature. The forward and backward spectra were fitted simultaneously to Eq. 3.10 with the Abragamian form for  $P_X(t)$  (Eq. 3.13a). As a first step all parameters were left free, three regions could be identified as shown in table 4.5. Then the asymmetries were fixed to the average value,  $\Delta\chi$  was held constant to the average on the plateau of the region and the data refitted. In table 4.5 in addition to the temperature range of the region, the average value of  $\Delta\chi$  and  $\tau_C$  on the plateau and the activation energy

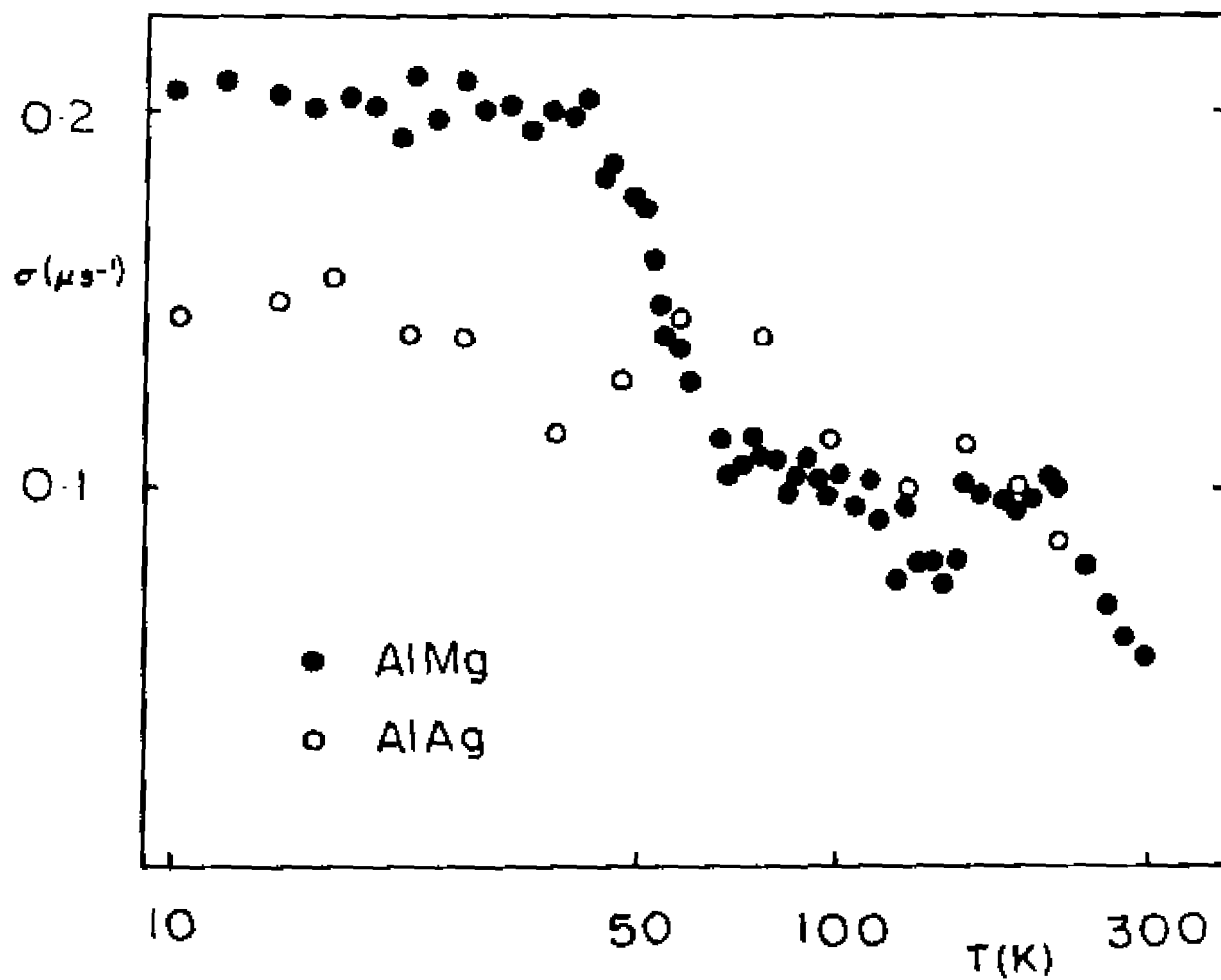


Figure 4.6  
 $\sigma(T)$  from BNL, 150G transverse field.

TABLE 4.6

$$\Delta X = \sqrt{(3/5)} \Delta Z \text{ (From Table 4.4)}$$

---



---

	$\Delta Z(QI) (\mu s^{-1})$	$\Delta X (\mu s^{-1})$
	10 % N.N. relaxation for T&O sites plus a correction term for the rest of the atoms.	strong field
T	0.369	0.286
O	0.289	0.224
V	0.203	0.157

---

calculated for the drop off ( Eq. 4.1, Fig. 4.7) are listed.

The zero and longitudinal field experimental depolarization were extracted from the forward spectrum using Eq. 3.20. Only the forward data were used because of the lower background. The data are presented in Fig. 4.8, also shown is the theoretically calculated depolarization from static fields for zero and 7G longitudinal field (Eq. 3.21b and Eq. 3.21a ).

Interpretation: The height difference between the damping rates at 150G Fig. 4.6 and 500G Fig. 4.2d is the result of contributions to depolarization from eqQ at 150G. Table 4.6 is a list of  $\Delta Z(QI)$  obtained from the data in table 4.4 by adding to the nearest neighbors result with 10% relaxation the difference between the results considering lattice sums and that of nearest neighbors with no relaxa-

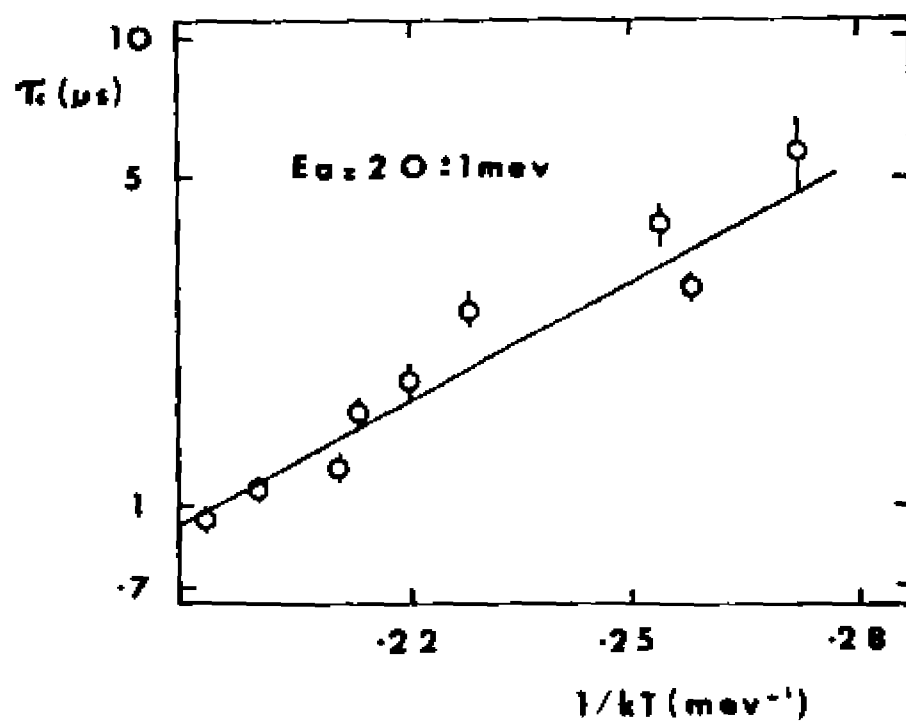


Figure 4.7  
 A plot of  $\text{Ln}\tau_c$  versus  $1/kT$  for Mg between 42K and 60K. The slope is the activation energy  $E_a$ .

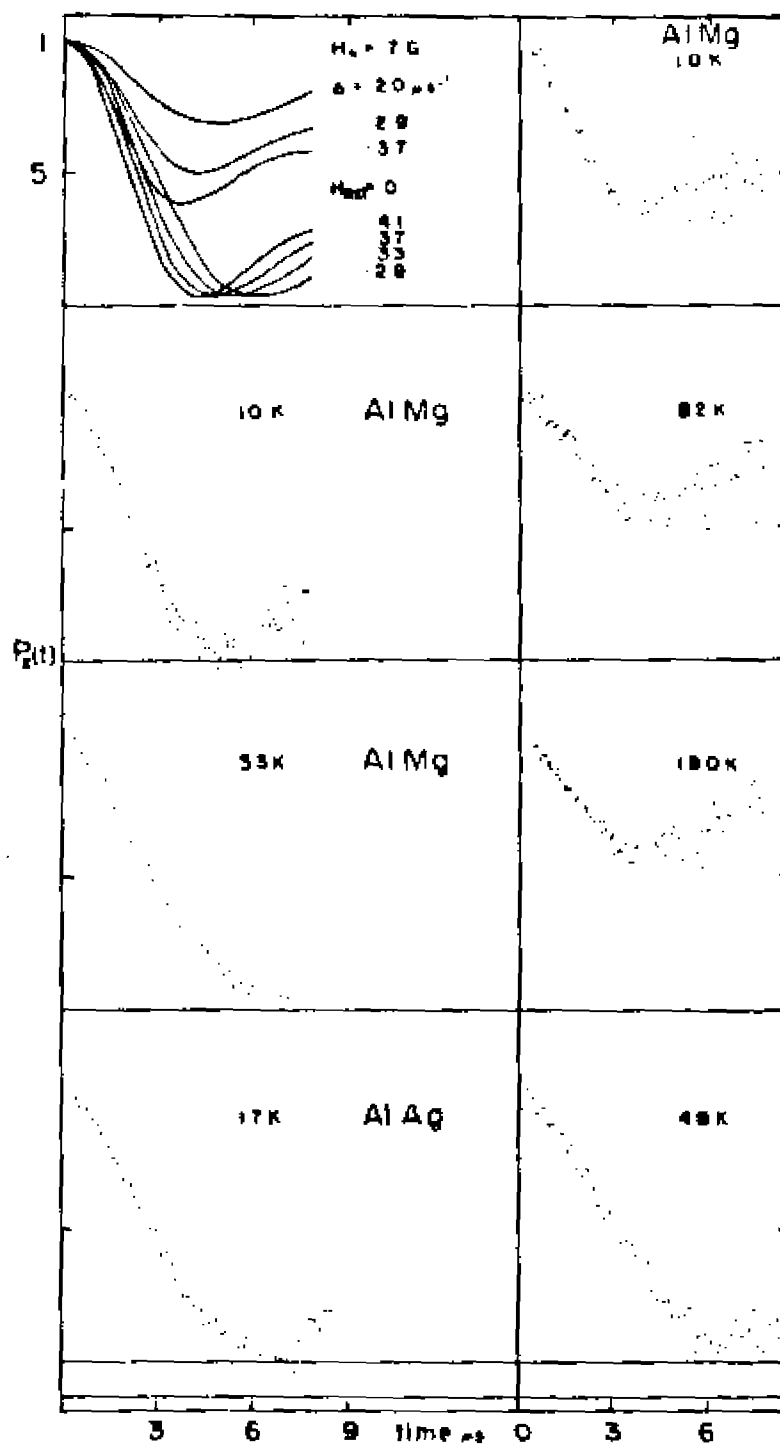


Figure 4.8  
Polarization versus time. The curves are calculated for a static field surrounding at zero and 7G, the data are from BNL on AlMg and AlAg.

tion. Finally  $\Delta_2 X$  for a strong transverse field was calculated from  $\Delta_X = \sqrt{(3/5)} \Delta_2$ .

As the temperature changes (compare tables 4.6 and table 4.5), signs of three different trapping sites are seen. Region I corresponds to a T-site trapping where the large  $\Delta_X$  obtained from the experimental data is the result of using 150G which was not large enough to completely decouple the eqQ. Region II can be an O-site trapping where the eqQ is weaker since the  $\mu^+$ -Al distance is larger than in the T-site or it can be a T-site trapping close to the impurity where lattice expansion reduces  $\Delta_X$ . Region III is vacancy trapping. The activation energy from vacancies in pure Al is between 23meV and 39meV<sup>26,27</sup>. The value for AlMg measured here is three times as large and is in agreement with the 82 meV reported by Hatano et al.<sup>27</sup>. According to the authors this large difference is the result of Mg-induced long range strain fields being felt at the vacancies.

The depolarization at 10K of the zero field data Fig. 4.8 matches well with  $\Delta_2 = 0.37 \mu s^{-1}$ . The tail section with few events is sensitive to background and therefore it should be given less weight. In general the tail falls below the function while the dip is higher and wider, implying some muon motion ( $\tau_C = 8 \mu s$ , table 4.5). Zero field runs were also taken at 24K and 42K, they look the same as the 10K run. The data at 53K have no recovery, which is a sign of muon diffusion out of traps. The longitudinal data show a clear change in height with temperature, in agreement with

changing trapping sites. The run at 180K is lower than the theoretical curve with  $\Delta_2 = 0.2 \mu\text{s}^{-1}$  indicating that there could be a mixture of two sites at that temperature.

#### E. AlAg<sub>1000</sub>ppm

Results: The same experimental procedure and data analysis as in the case of AlMg were used here. The values of  $\Delta_x$  around the two peaks were on the order of  $0.22 \mu\text{s}^{-1}$ ,  $\tau_C$  was on the order of  $8 \mu\text{s}$  and  $E_a$  for the first drop off = 6 meV. Two zero field runs done at 17K and 48K are shown in Fig. 4.8.

Interpretation: The zero field data at 17K have some recovery at  $t=6\mu\text{s}$  (Fig. 4.8) matching the curve with  $\Delta_2 = 0.29 \mu\text{s}^{-1}$ , this corresponds to an O-site trapping in agreement with the results of the transverse field Abragamian fits (section 4.3E). Since no recovery is observed in the zero field data at 48K the muon is expected to be moving at this temperature, this is in agreement with the  $\sigma(T)$  plot (Fig. 4.6).

#### 4.4 SUMMARY

To understand the nature of the trapping centers it is important to know the perturbations a defect causes in the crystal. The macroscopic strain effect of introducing Cu in Al is to contract the lattice, Mg will expand it while Ag and Zn have little effect (table 4.2 and Fig. 4.3). On the other hand the electronic interaction is stronger for Cu and Ag than Mg and Zn in Al (Fig. 3.8).

Zn, with very little of both interactions, should and does (Fig. 4.2e) have the least structure in the damping rate temperature dependence.

Ag, with only the electronic interaction has a trapping peak at about 17K which is a higher temperature than the position of the first peak due to other impurities; also the trapping site is an O-site compared to a T-site for Mg and Cu. Therefore the first peak (17K) is the result of trapping due to the short range electronic attraction.

Mg has a high and wide trapping peak starting at about 10K, the peak for Cu rises like Mg but it is narrower. Therefore trapping in both cases results from the long range strain fields and it depends on the magnitude but not sign of deformation. The local contraction due to the Cu impurity yields repulsive sites close to the impurity resulting in a narrow peak. while the width of the Mg peak is due to possible trapping close to the impurity caused by local lattice expansion produced by the Mg atom.

The vacancy peaks ( peaks on the high temperature side of Fig.4.2) for Zn and deformed Al are almost at the same temperature, whereas for Mg it is at a higher temperature, and for Cu it is even at higher temperatures. This correlates very well with the long range strain fields given in (table 4.2).

Therefore in an Al lattice with point defects, two regions can be identified. The first is beyond the range of

the extended trapping centers, where muon diffusion results from one phonon processes and reflects the properties of a pure crystal. The second is the trapping centers around impurities which in turn can be divided into two regions. Far from the defect the dominant effect is due to symmetry breaking by the long range strain fields. Impurities that expand or contract the lattice will have direction dependent attractive sites in this region. The idea of direction dependent attractive sites is in agreement with the results of continuum theory for the interaction of two point defects as described in section 3.3C. Closer to the impurity ( $< 4A$ ) both interactions have to be considered. Elastically the sites are attractive if the impurity expands the lattice locally (Mg in Al), while they will be repulsive if it contracts the lattice (Cu in Al). This agrees with lattice static calculations for H-impurity interactions, also described in section 3.3C. The elastic interaction is the dominant force in the case of Mg or Cu in Al. The electronic interaction depends on the valence and core radius of the impurity (section 3.2), Ag in Al traps positive muon at O-sites by this interaction.

Chapter V  
UNIAXIAL STRESS-INDUCED SYMMETRY BREAKING  
OF MUON SITES IN IRON

5.1 OVERVIEW

The local field seen by a muon in a ferromagnetic metal  $B_{\mu}$  is given by Eq. 3.6a and Eq. 3.6b (section 3.1C). Because interstitial sites in BCC metals have tetragonal symmetry (section 3.2) the structurally equivalent O(T) sites are magnetically inequivalent in Iron. There are twice as many O sites with  $B_{dip.}^{\prime} = -9.25$  kG as those with  $B_{dip.}^{\prime} = 18.5$  kG, and the T sites with  $B_{dip.}^{\prime} = 2.6$  kG are twice as many as those with  $B_{dip.}^{\prime} = -5.2$  kG (Fig. 5.1). Rapid muon diffusion between the sites averages the dipolar field (last term in Eq. 3.6b) to zero, leading to the single muon precession frequency observed in  $\mu$ SR experiments.

This chapter is a study of the muon interaction with an Fe lattice in which uniaxial stress along the  $\langle 100 \rangle$  direction, also the axis of magnetization, splits the degenerate energy states between O(T) sites (Eq. 3.32, section 3.3D). This results in a statistical population shift between the magnetically inequivalent sites and leads to a change in the average field sensed by the muons, which is observed as a shift in muon precession frequency.

The change in the average magnetic field seen by the

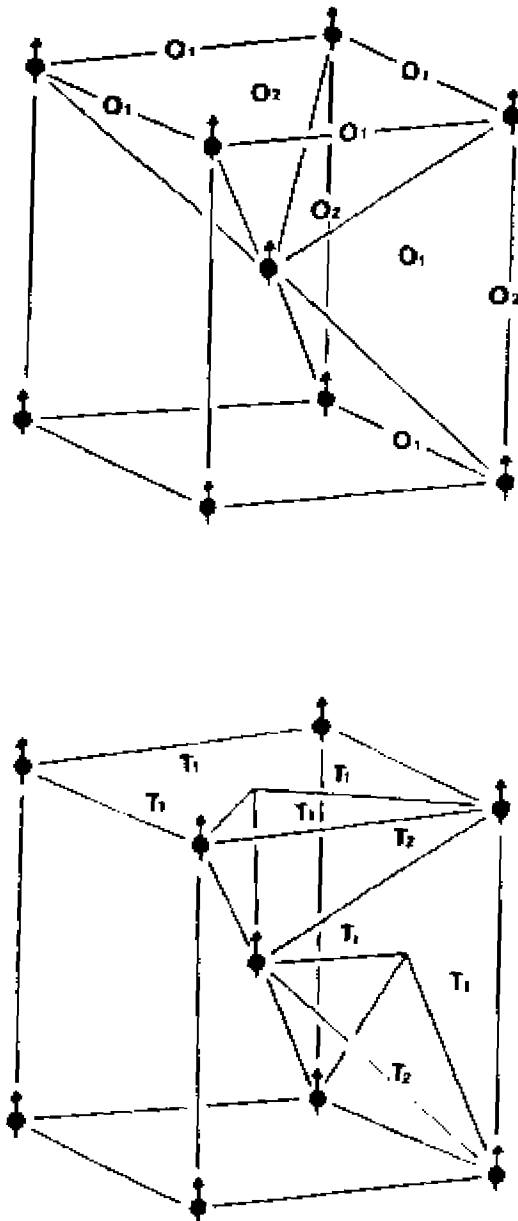


Figure 5.1

BCC structure of Iron. The arrows represent the magnetic dipole moments carried by the ions. The dipolar fields at  $O_1, O_2, T_1$  and  $T_2$  are  $-9.26$  kG,  $18.52$  kG,  $2.63$  kG and  $-5.25$  kG respectively. There are twice as many  $O_1(T_1)$ -sites as there are  $O_2(T_2)$ -sites.

muons due to their population shift can be written as,

$$\Delta B_{\mu}' = \frac{[ 2 B_{\text{dip}.1}'(T) e^{-E_1/kT} + B_{\text{dip}.2}'(T) e^{-E_2/kT} ]}{[ 2 e^{-E_1/kT} + e^{-E_2/kT} ]} \quad (5.1)$$

where the subscripts 1 and 2 refer to the two magnetically inequivalent sites and  $T$  is the temperature. Multiplying the numerator and denominator by  $e^{E_1/kT}$  and using series expansion with the assumption that:  $B_{\text{dip}.i}'(T) = B_{\text{dip}.i}'(0) M_S(T)/M_S(0)$  and  $|\Delta E| = |E_1 - E_2| \ll kT$ , Eq. 5.1 to first order can be written as,

$$\Delta B_{\mu}' = - 2/3 B_{\text{dip}.1}'(0) M_S(T)/M_S(0) \Delta E/kT \quad (5.2)$$

The first uniaxial stress experiment was done at room temperature on a pure Fe single crystal using surface muons at the Swiss Institute for Nuclear research (SIN). The change in the local field was measured and an order of magnitude agreement with experiment was obtained by using the results of Sugimoto and Fukai<sup>28</sup> on muons in Nb and V to estimate  $\Delta E$  for Fe (Namkung et al.)<sup>17</sup>. To confirm the above model additional work has been done at room temperature and 360K on Fe(3 wt. % Si) at BNL. In this chapter, the experimental detail of the work at BNL will be described and the results listed and discussed. For comparison mention will be made of the experiment at SIN. Most of the material in this chapter has been published in a paper by Kossler et al.<sup>29</sup>

Table 5.1  
 Properties and  $\mu$ SR results of Iron (Fe)

---



---

Structure	BCC
Lattice constant a(room temperature)	2.87 Å
$C_{11}$ at room temperature	$2.26 \cdot 10^{12}$ dynes/cm <sup>2</sup>
Saturation magnetization*	
$M_S(0K)$	1.750 kG
$M_S(300K)$	1.688 kG
$M_S(360K)$	1.658 kG
Local field at muon $B_U(0K)$	$-3.67 \pm 0.10$ kG
Hyperfine field $B_{hf}(0K)$	$-11.1 \pm 0.2$ kG
Calculated dipolar fields ( $B_{dip.1(2)}$ 0K)	
O	$-9.26$ (18.52) kG
T	$2.63$ (-5.25) kG
Muon site	O & T sites**

---

\* Fig. 5.2 shows  $M_S$  as a function of temperature

\*\* Section 5.3 of this work.

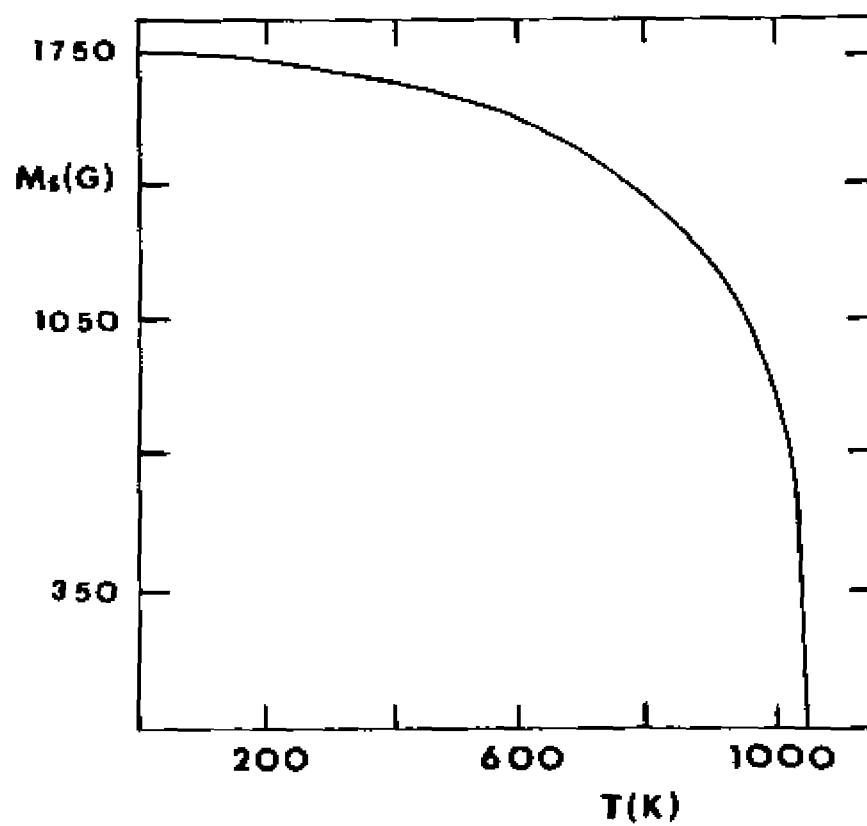


Figure 5.211  
The saturation magnetization versus temperature for pure Fe,  
 $M_s(0K) = 1750$  G.

## 5.2 EXPERIMENT

### A. Samples

The samples were supplied by Monocrystals Co. of Cleveland Ohio. The Fe(3 wt. % Si) single crystal was grown in vacuum by the Bridgman method from a powder mix, prepared from iron (99.52 % Fe, 0.04 % H, 0.04 % C and 0.05 % others) and Si powder. The  $\langle 100 \rangle$  axis was determined by X-ray and the sample cut using thin abrasive saws and point mills. Chemical etching was used to clean the surfaces. The dimensions of the sample were  $2.8 \times 10 \times 50 \text{ mm}^3$ , with the long axis being the  $\langle 100 \rangle$ , and the  $\langle 010 \rangle$  axis is  $14^\circ$  from the wide surface perpendicular. Grooves 2mm wide and 1mm deep were cut in the wide surface 2mm from the ends using an electro-discharge milling machine at BNL. The pure iron sample had the following dimensions  $1 \times 4.6 \times 46.13 \text{ mm}^3$ , with the long axis being the  $\langle 100 \rangle$  direction. The difference in the intensities of the two muon beams used in this study made it necessary to work with a larger sample at BNL.

### B. Beams

The in-flight decay beam at the AGS of BNL was used to study the Fe(3 wt. % Si) single crystal. For 1 TP on the production target per AGS cycle the event rate was 350 resulting from 1800 muon-stops in the sample. One million events were collected, corresponding to about two and a half hours per run. A surface muon beam was used at SIN, and three

million events were collected per run.

### C. Pulling Apparatus

In order to prevent misalignment and minimize mechanical strain a jig and sample support were used to mount the sample. Fig. 5.3 shows the puller constructed at the machine shop of the physics department, College of William and Mary. Epoxy was used to hold the crystal to the sample holders which were then held by screws to the rods of the puller (Fig 5.3). One of the rods was free to slide in and out according to the applied stress. The epoxy used softened at 360K which necessitated the cutting of grooves in the sample to mate ridges in the holders.

### D. Temperature

All temperature measurements were made with a Pt resistor held in place between a pair of the sample holders by conductive grease. For the Fe(3 wt. % Si) at 300K the temperature was nearly constant without control. The 360K was maintained by circulating temperature controlled hot water through the cooling and heating lines. Due to melting of the conductive grease around the Pt resistor at 360K and the motion of the holders associated with the maximum stress on-off point a temperature difference occurred between the Pt resistor and the sample. This error was estimated to be 3K and the data has been corrected for it. For the pure Fe sample 302K was maintained by circulating ethanol at a

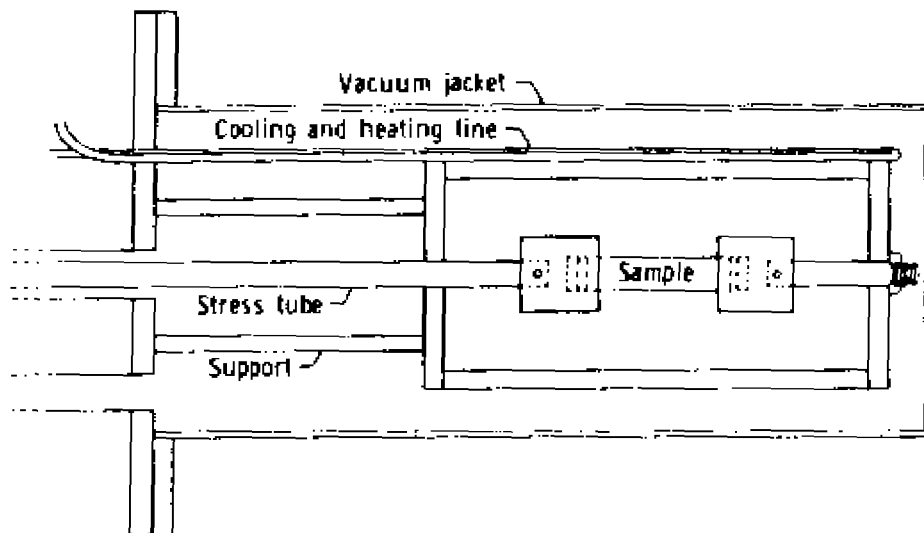


Figure 5.3  
The pulling apparatus (Puller). The sample shown is the Fe(3 wt. % Si) which was 5 cm long and 1 cm wide.

Table 5.2

Calculation of  $S_{11}$  and  $S_{12}$ , Megabars =  $10^{12}$  dynes/cm<sup>2</sup>

	298K	373K	360K
$C_{11}^{30}$ (Mb)	2.26	2.22	2.23
$C_{12}^{30}$ (Mb)	1.40	1.32	1.33
$S_{11}^*$ (Mb <sup>-1</sup> )	0.84		0.80
$S_{12}^{**}$ (Mb <sup>-1</sup> )	-0.32		-0.30

$$* S_{11}^{16} = 1/3 (C_{11} + 2C_{12})^{-1} + 2/3 (C_{11} - C_{12})^{-1}$$

$$** S_{12}^{16} = 1/3 (C_{11} + 2C_{12})^{-1} - 1/3 (C_{11} - C_{12})^{-1}$$

constant temperature.

#### E. Strain

Strain was induced in the samples by uniaxial stress in the <100> direction applied by dead weights in the case of Fe(3 wt. % Si) and by a piston and compressed air for the pure Fe. At 300K and 302K strain was measured directly by using strain gauges. At 360K strain was found for a certain weight (stress) by scaling linearly  $C_{11}$  and  $C_{12}^{30}$  to 360K then calculating  $S_{11}(300K)$  and  $S_{11}(360K)$  (table 5.2), and finally evaluating the strain from the following relation  $e_{xx}(360K) = [S_{11}(360K)/S_{11}(300)] e_{xx}(300)$ . Table 5.3 lists the stress-strain correspondence used in the case of Fe(3wt.%Si).

Table 5.3  
Stress-strain in <100> direction

Weight	$e_{xx}$ (microstrain)	
	300K	360K
29.5	82.4	78.6
59.2	169.6	161.9

#### F. Data Analysis

The following function was used to fit the forward and backward histograms simultaneously in the case of the pure Fe data.

$$N_{F/A}(t) = N_{0F/A} e^{-t/\tau} (1 \pm p \{F_1 e^{-t/T1} + F_2 e^{-t/T2} \cos(\omega_\mu t + \phi)\}) + \text{Bkgd}_{F/A} \quad (5.3)$$

It includes the effect of longitudinal as well as the transverse domain polarization with respect to the muon spin direction. When T2 was short, replacing  $e^{-t/T2}$  by  $e^{-\sigma^2 t}$  significantly reduced  $\chi^2$ .

In-flight muons have higher energy than surface muons. Therefore they stop in the bulk of the sample and do not interact with surface defects. For this reason  $F_2/F_1$  was always large in the case of data taken at BNL and therefore

Eq. 5.3 can be written as,

$$N_{F/A}(t) = N_{0F/A} e^{-t/\tau_\mu} (1 \pm a e^{-\sigma^2 t^2} \cos(\omega_\mu t + \phi)) + \text{Bkgd}_{F/A} \quad (5.4)$$

which was used to fit the Fe(3% wt. Si) data.

#### G. Magnetic Domain Alignment

The experimental results are dependent on the orientation of the domains with respect to the stress axis. Fig. 5.4a,b indicates  $\omega_\mu$  as a function of  $B_{\text{ext}}$ , as can be seen the field penetrates above 120G for the Fe and 350G for the Fe(3 wt. % Si) samples, implying saturation. The drop in  $\omega_\mu$  is due to the fact that the internal field is opposite to the externally applied field.

In the case of the Fe(3 wt. % Si) the uniform stopping beam of the AGS was used, therefore fitting was done with Eq. 5.4. The experiment was run at 325G. At higher fields the non-ellipsoidal shape induced field inhomogeneities and therefore faster depolarization (Fig 5.6), which means less accuracy in frequency determination.

For the pure Fe sample the experiment was done at 150G with a surface muon beam. Due to the muons' low energy they stopped close to the surface where the domains were naturally not completely aligned along the easy axis giving rise to field inhomogeneities in this region. The data were fitted to Eq. 5.3 which gives a more direct measure of alignment,  $F_t/F_1$  as shown in Fig. 5.5.

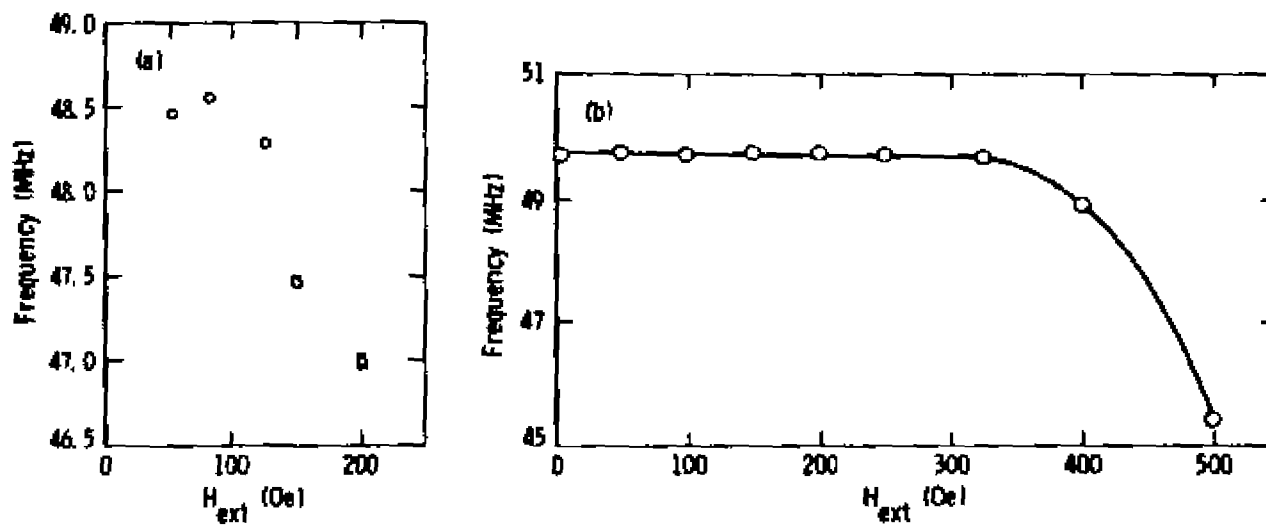


Figure 5.4  
Precession frequency versus applied field along the long axis of the samples. (a) Pure Fe at 302K<sup>17</sup> (b) Fe(3 wt. % Si) at 300K. The experiment was done at (a) 150 G (b) 325 G.

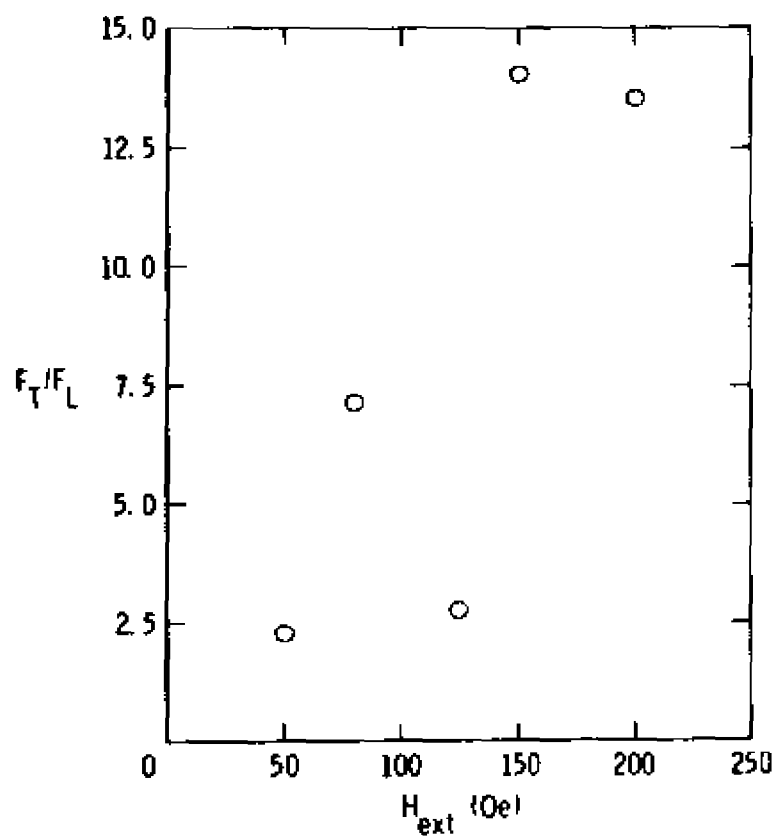


Figure 5.517  
 $F_t/F_L$  (measure of domain alignment) versus applied field for pure Fe.

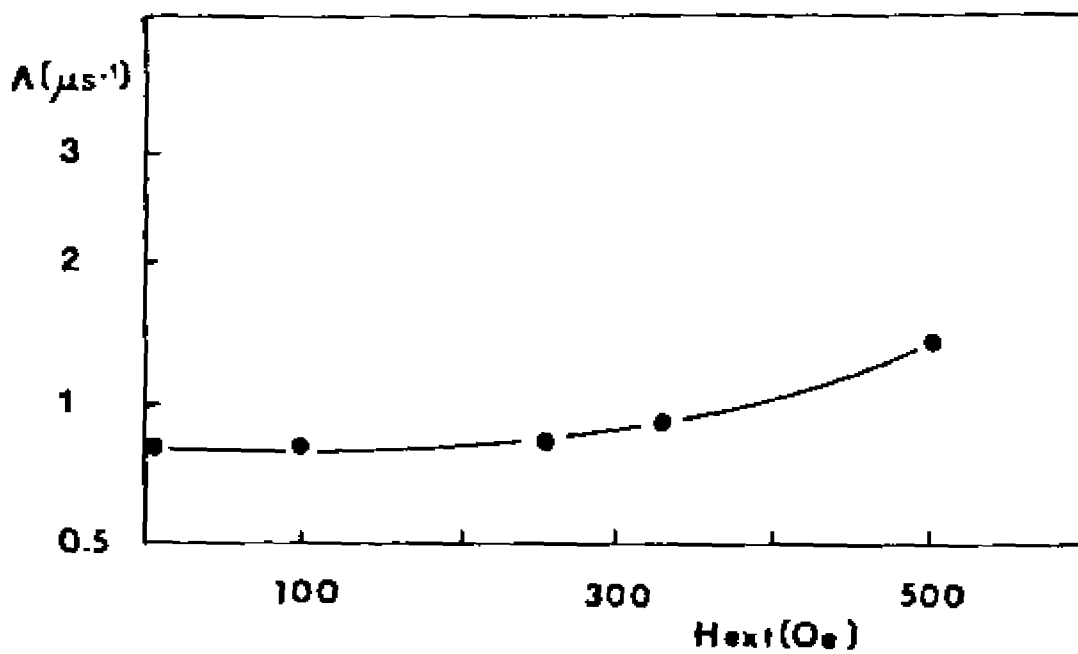


Figure 5.6  
Depolarization rate for Fe(3 wt. % Si) versus applied field.  
 $P(t) = \text{EXP}(-\lambda^2 t^2)$ .

Table 5.4

Change in frequency and field with strain and temperature

	Fe	Fe(3 wt. % Si)	
	302K	300K	360K
$df/de$ (MHz/100 $\mu\epsilon$ )	$-0.34 \pm 0.023$	$-0.348 \pm 0.007$	$-0.279 \pm 0.010$
$dB_{\mu}/de$ (G/100 $\mu\epsilon$ )	$25.1 \pm 1.6$	$25.7 \pm 0.5$	$20.6 \pm 0.7$

### 5.3 RESULTS and DISCUSSION

Fig. 5.7 shows the muon precession frequency in (a) pure Fe at 302K, (b) and (c) Fe(3 wt. % Si) at 300K and 360K respectively, as a function of strain along the  $\langle 100 \rangle$  axis of the crystal. To check the reversibility, stress-off points were taken after each stress-on run. These frequencies are constant and are shown along a line parallel to the horizontal. The results of a straight line fit to the points are given in table 5.4.

The sign difference between the frequency and field shifts is due to the fact that  $B_{\mu}$  and  $B_{ext.}$  are antiparallel. That the stress-off points correspond to a constant frequency implies that elastic history effects do not enter. The agreement at room temperature of the shifts observed for pure Fe and Fe(3 wt. % Si) indicates that these effects are intrinsic to the pure crystal properties and not impurity

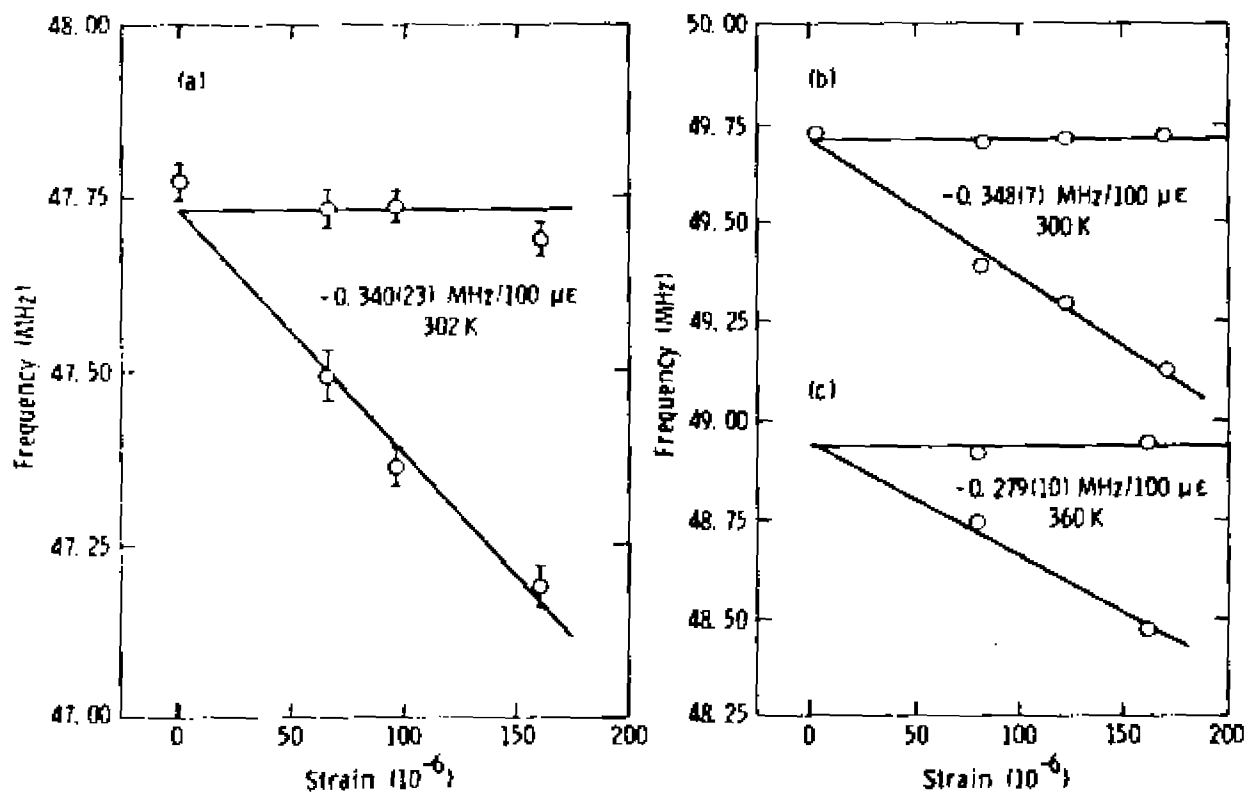


Figure 5.7  
Precession frequency for (a) Pure Fe at 302K<sup>17</sup>, (b) Fe(3 wt. % Si) at 300K and (c) Fe(3 wt. % Si) at 360K, as a function of strain. The points parallel to the horizontal are stress-off points after each stress-on point (Elastic history does not enter).

dependent. The frequency accuracy for Fe(3 wt. % Si) with one million events per run is better than that of pure Fe with three million events per run. This is a reflection of a slower depolarization rate, which results from: 1) The more homogeneous fields deeper in the sample and 2) the less internal strain resulting from the greater ease with which the alloy could be annealed, since there is no phase transition upon cooling from the melting point.

The derivative of  $B_\mu$  with respect to strain is,

$$\begin{aligned} dB_\mu/d\epsilon_{100} = & dB_{\text{ext.}}/d\epsilon_{100} + dB_{\text{dem.}}/d\epsilon_{100} + dB_L/d\epsilon_{100} + \\ & dB_{\text{hf.}}/d\epsilon_{100} + dB_{\text{dip.}}/d\epsilon_{100} \end{aligned} \quad (5.5)$$

$dB_{\text{ext.}}/d\epsilon_{100} = 0$ . The demagnetizing field is about 125G for pure Fe and 325G for the Fe(3 wt. % Si), its fractional change with strain is on the order of the strain, for  $100\mu\epsilon$  it should be about 0.01G and can be ignored.

For the Lorentz field ( $B_L = 4\pi/3 M_S$ ) let us consider the following thermodynamics equation<sup>31</sup>  $(d\lambda_S/dH)_{\sigma,T} = (dM_S/d\sigma)_{H,T}$ , where  $\lambda_S$  is the saturation magnetostriction along the direction of the external field.  $(d\lambda_S/dH)_{H,T}$ <sup>32</sup> =  $2.3 \times 10^{-10}/G$  along the  $\langle 100 \rangle$  axis of pure Fe crystal at room temperature. Therefore  $(dM_S/d\sigma)_{H,T} = 2.3 \times 10^{-10} G/(\text{dynes}/\text{cm}^2)$ ,  $d\sigma_{XX}/d\epsilon_{XX} = C_{11} = 2.3 \times 10^{12} \text{ dynes}/\text{cm}^2$  for pure Fe at room temperature. For  $100 \mu\epsilon$ ,  $\Delta M_S \approx 0.05G$ , hence the contribution of  $dB_L/d\epsilon_{100}$  ( $\approx 0.2 G/100\mu\epsilon$ ) can be neglected. Jena et al.<sup>33</sup> estimated the change in  $B_L$  from measured changes in magnetization under

pressure and compressibility to be 0.3 G/100 $\mu\epsilon$ .

The change in the hyperfine field induced by uniaxial strain arises from the dependence on the distance from nearby Fe atoms. From the homogeneous pressure results of Butz et al.<sup>34</sup>  $d(\ln B_{hf.})/d(\ln V) = +0.92(1)$ ,  $\Delta B_{hf.} = 0.92 \Delta V/V B_{hf.} \approx -3G$  for a positive volume strain of  $300 \times 10^{-6}$ , which corresponds to 100  $\mu\epsilon$  uniaxial strain. Since the atoms along the stress axis move out while those along the perpendicular move in  $dB_{hf.}/de_{xx} (= -1G/100\mu\epsilon)$  is small and can be left out.

$\delta B_{dip.}'/de_{100}$  arises from two effects: 1) The change in the occupation probabilities (Eq. 5.2). 2) The sum of  $B_{dip.}'$  over O(T) sites does not equal zero any more, this is due to lowering of the sites symmetry by uniaxial stress.

$$\Delta B_{\mu} = - \frac{2}{3} B_{dip.1}'(0) M_S(T)/M_S(0) \Delta E/kT + \frac{1}{3} (2B_{dip.1}' + B_{dip.2}') \quad (5.6)$$

Estimates for  $B_{dip.1}'$  and  $B_{dip.2}'$  are dependent on the lattice sites, lattice distortion and the muon wave function (table 5.5). Eq 5.6 can be written in the following form,

$$\begin{aligned} \Delta B_{\mu}' &= \Delta B_{\mu} - \frac{1}{3} (2B_{dip.1}' + B_{dip.2}') \\ &= - \frac{2}{3} B_{dip.1}'(0) M_S(T)/M_S(0) \Delta E/kT \quad (5.7) \end{aligned}$$

In table 5.7 we list  $\Delta B_{\mu}'$  G/100 $\mu\epsilon$  at room temperature calculated from Eq. 5.7 using  $\Delta E$  meV/100 $\mu\epsilon$ , obtained from:

Table 5.5

$B_{dip,1}^i (= -1/2 B_{dip,2}^i)$  under various conditions at T=0K

		O	T	
1	- Point-like muon, rigid lattice	-9.25	2.6	kG
2**	- Point-like muon, nearest neighbors relaxation scaled from Nb and V	-6.75	1.85	kG
3**	- Spherical muon wave function*, ( $\alpha =$ $\beta = 0.15(0.19)$ ) and relaxation	-6.5	1.85	kG
4**	- Oblate wave function to match muon in O site Nb or V, ( $\alpha = 0.19, \beta = 0.15$ )	-4.65		
5**	- Prolate wave function to match muon in T site Nb or V, ( $\alpha = 0.19, \beta = 0.25$ )		2.4	kG
6***	- Point-like and relaxation	-5.6	2.2	kG
7***	- Wave function and relaxation	-3.8	2.2	kG
8***	- $1/3 (2B_{dip,1}^i + B_{dip,2}^i) / 100 \mu e$			
	Point like	-7.1	-2.3	G
	Wave function and relaxation	-2	-1	G

\*  $|\psi_{\mu}(r)|^2 = [1/\alpha^2 \beta \pi^{3/2}] \text{EXP}\{-(x^2+y^2)/\alpha^2 - z^2/\beta^2\}$

\*\* Namkung et al.<sup>17</sup> or Kossler et al.<sup>29</sup>

\*\*\* Jena et al.<sup>33</sup>

Table 5.6

 $(P_d - P)$  eV for Fe extrapolated from Nb

	3.3A	2.87A
O	3.466	3.73
T	- 1.075	- 1.23

a) The calculations of Jena et al.<sup>33</sup>

b) Extrapolating the results of Sugimoto and Fukai<sup>28</sup> on Nb to find the difference in the double force tensor diagonal elements for Fe. They report a linear change of 5.3% for O and 9.7% for T sites upon decreasing the lattice parameter from 3.3A to 3A. Using the lattice parameter for Fe,  $(P_d - P)$  can be estimated (table 5.6).  $\Delta E$  can then be calculated from Eq. 3.32.

c) Reversing the  $\Delta E$  of Jena et al.<sup>33</sup> while keeping the signs.

Included in table 5.7 are the average of  $\Delta B_{\mu} / 100\mu\epsilon$  assuming equal occupation of O(T) sites weighting them with 1(2), (there exist twice as many T sites as there are O sites in a BCC lattice.) and the experimental result after adding a correction to account for the new atomic positions associated with strain.

TABLE 5.7

$\Delta B_{\mu}$  ' G/100 $\mu$ e,  $\Delta E$  meV/100 $\mu$ e, weights for average 1(2) for O(T) sites

	O		T		Average
	$\Delta B_{\mu}$ '	$\Delta E$	$\Delta B_{\mu}$ '	$\Delta E$	$\Delta B_{\mu}$ '
Jena et al. <sup>33</sup>	18	0.19	29	- 0.53	25.3
$\Delta E$ from Nb field from table 5.4 (4)&(5)	60	0.52	10.1	- 0.17	26.7
Reverse of $\Delta E$ of Jena et al. <sup>33</sup>	50	0.53	10.4	- 0.19	23.6
Experiment					27 $\pm$ 5

Our room temperature result is in reasonable agreement with the first-principles self-consistent calculations of Jena et al.<sup>33</sup> and with the extrapolations to Fe from the results of Sugimoto and Fukai<sup>28</sup> for Nb. We have assumed equal occupation of O and T sites which is consistent with the nearly equal energy reported by Jena et al.<sup>33</sup> for the two sites.

The left side of Eq. 5.7 (term due to the population shift) is proportional to  $M_B(T)/T$ , using the data from table 5.1 the following ratio will be expected:  $[M_B(300)/300]/-[M_B(360)/360] = 1.22$ . On the right hand side weighting the correction to  $\Delta B_{\mu}$  (table 5.5) by 1(2) for O(T) sites gives

-1.33, therefore the ratio from the data is  $\{25.7+1.33\} / \{20.6+1.33\} = 1.23$  in agreement with expectation.

We attempted to measure the frequency shift below room temperature, but as a result of the very fast depolarization (compare Fig. 5.8a & b or Fig.5.9) the frequency could not be determined with reasonable accuracy.

#### 5.4 SUMMARY

Uniaxial stress was applied to Fe and Fe(3wt. % Si) single crystals and the induced muon-precession-frequency-shifts were measured as a function of strain. The same shift per  $100\mu\epsilon$  was observed for both samples at 300K, this implies that these effects are intrinsic to the pure lattice. The magnitude of the shifts at 300K and 360K are in good agreement with theoretical predictions and extrapolation from Nb and V, especially if both O and T sites are equally probable. Their  $(1/T)$  temperature dependence implies that the dominant effect is that of the strain-induced-population-shift between crystallographically equivalent, but magnetically inequivalent sites.

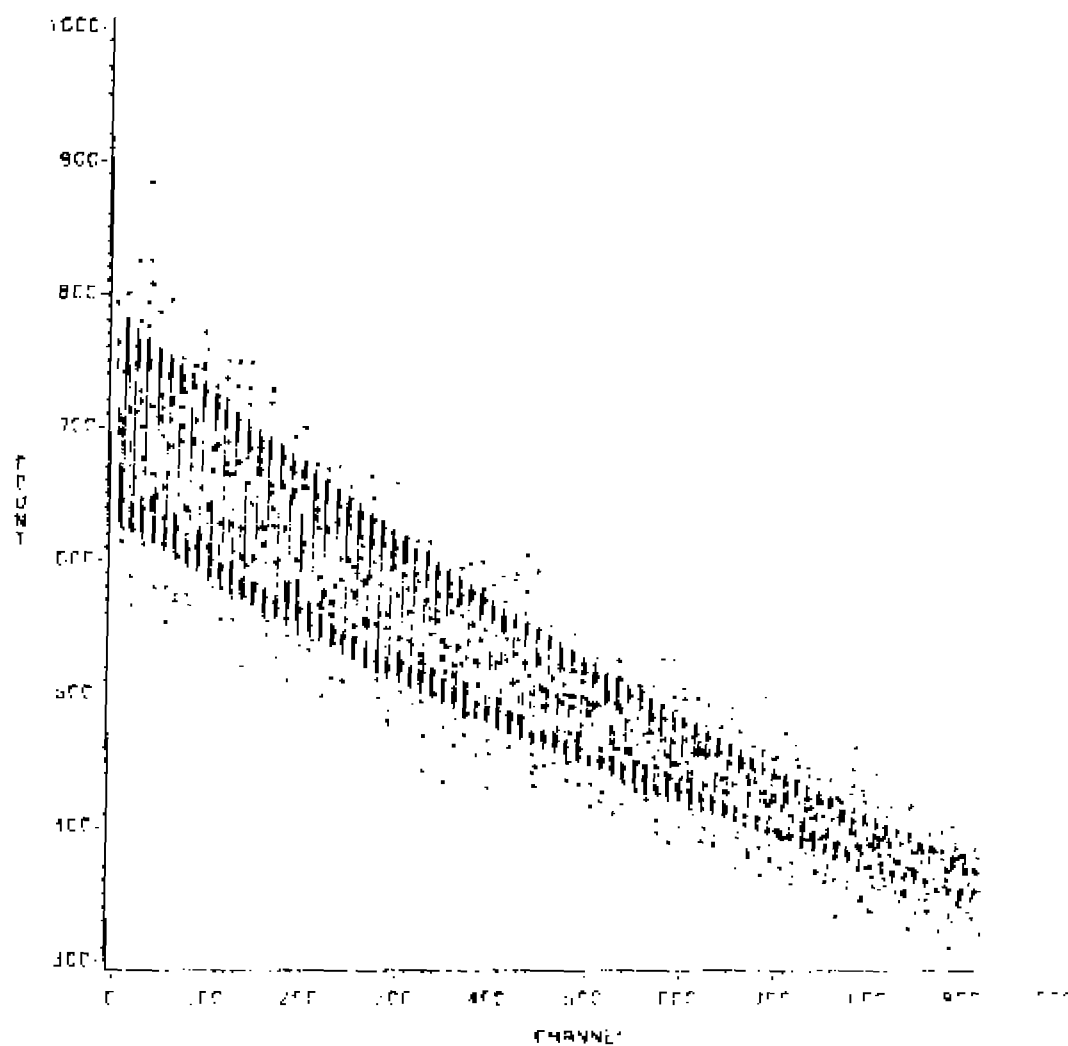
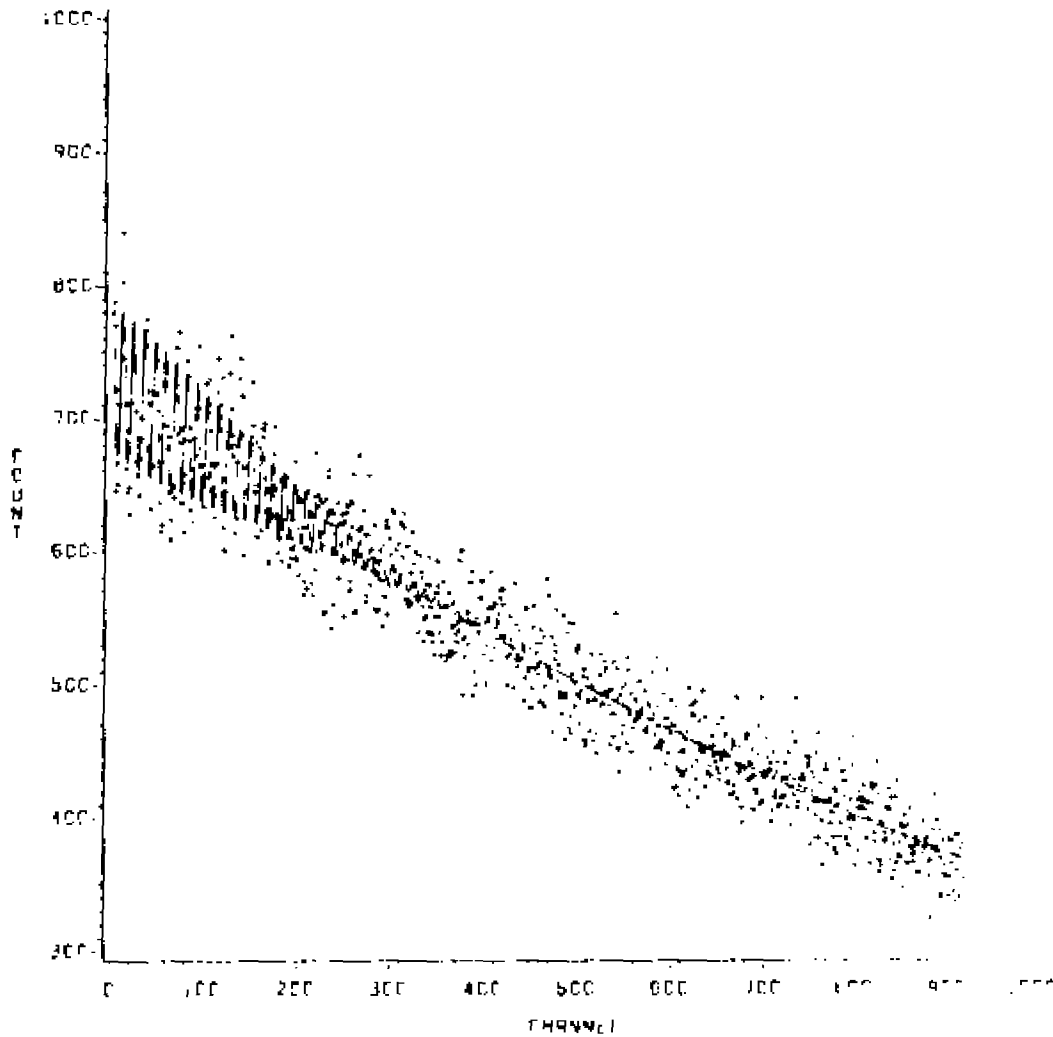


Figure 5.8a  
 $\mu$ SR data (points) from the Fe(3 wt. % Si) experiment taken at 360 K. 128 channels correspond to 0.22  $\mu$ s. Also shown is the fit using Eq. 5.4 (solid line).



**Figure 5.8b**

Except for the temperature ( 215K ) the situation is the same as in figure 5.8a. Notice how fast the signal disappears.

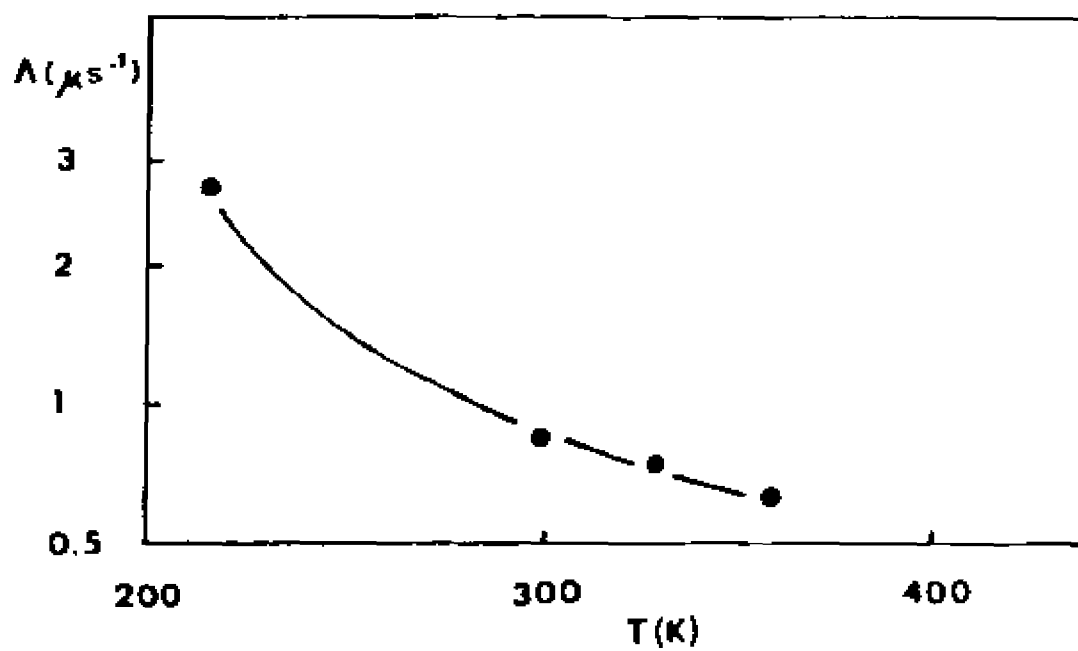


Figure 5.9  
The depolarization as a function of temperature for the Fe(3 wt. % Si).

## CONCLUSION

The importance of the elastic interaction in determining the muon state in metal, in the presence of other point defects or a more extended strain field like uniaxial stress, has been demonstrated.

In the case of impurities in Aluminum we provided a general qualitative picture in which the elastic interaction dominates in AlCu and AlMg but not AlAg. Ca and to a lesser degree Ga and Ge in Al expand the lattice locally, therefore it will be very interesting for future experiments to look in these systems for the wide trapping peak observed in AlMg. If single crystals of the above systems are available, then field dependent studies should be done to determine the muon trapping site.

For Fe, by measuring the strain induced frequency shift at 300K and 360K we confirmed its  $(1/T)$  dependence, which implies that uniaxial stress induces a muon population shift between magnetically inequivalent sites. Future experiments should be performed for strain along other directions and for different materials, for example  $Fe_3Si$  or  $Fe_3Al$ .

## APPENDIX A

### Z-Component of Nuclear Dipolar Field

The nuclear dipolar field at the origin from an i-th point dipole  $u$  located at  $r$  is given by (Fig 3.4, Page 28),

$$H = \frac{u}{r^3} [3(\hat{u} \cdot \hat{r})\hat{r} - \hat{u}]$$

where

$$\hat{r} = x \sin\theta \cos\phi + y \sin\theta \sin\phi + z \cos\theta$$

$$\hat{u} = x \sin\epsilon \cos\phi + y \sin\epsilon \sin\phi + z \cos\epsilon$$

Its z-component can be written as,

$$H_z = H \cdot \hat{z}$$

$$= \frac{u}{r^3} [(3 \cos^2\theta - 1) \cos\epsilon + 3 \cos\theta \sin\epsilon \sin\phi \cos(\phi - \phi)]$$

$\phi$  can be set to zero without any loss of generality, this is equivalent to taking  $r$  to lie in the  $xz$ -plane. then,

$$H_z = \frac{u}{r^3} [(3 \cos^2\theta - 1) \cos\epsilon + 3 \cos\theta \sin\epsilon \sin\phi \cos\phi]$$

APPENDIX B  
Two State Model<sup>14</sup>

If the trapping (escape) rate is  $\nu(\epsilon)$ , the probability of the muon surviving untrapped (trapped) until time  $t'$  ( $t''$ ) and trapping (escaping) during the interval  $dt'$  ( $dt''$ ) is  $e^{-\nu t'} \nu dt'$  ( $e^{-\epsilon t''} \epsilon dt''$ ). The polarization function that include no-trapping, one-trapping--no-escape, one-trapping--one-escape, etc. all starting from the free state is:

$$P(t) = e^{-\nu t} P_0(t) + \nu \int_0^t dt' e^{-\nu t'} e^{-\epsilon(t-t')} P_1(t-t') \\ P_0(t') + \epsilon \int_0^t dt'' \nu \int_0^{t''} dt' e^{-\nu t'} e^{-\epsilon(t''-t')} \\ P(t-t'') P_1(t''-t') P_0(t')$$

where  $P_0(t)$  is the polarization function in the free state. As long as the depolarization in the free state is slow compared to the trapped state we can use  $P_0(t)=1$  in the above equation.

$$P(t) = e^{-\nu t} + e^{-\epsilon t} \nu \int_0^t dt' e^{-\bar{\nu} t'} P_1(t-t') + \\ \epsilon \int_0^t dt'' e^{-\epsilon t''} P(t-t'') \nu \int_0^{t''} dt' e^{-\bar{\nu} t'} P_1(t''-t')$$

Where  $\bar{\nu} = \nu - \epsilon$  and  $P_1(t)$  is the polarization function in the trapped state. Eq. 3.21a and Eq. 3.21b are used for  $P_1(t)$  for longitudinal and zero field respectively.

## REFERENCES

1. Proc. of the Yamada Conf. VII, Muon Spin Rotation, Shimoda, Japan, 1983. Edited by T.Yamazaki and K.Nagamine  
Hyp. Int. 17-19 (1984)
2. Muon Spin Research. Japan Society for the Promotion of Science (1979). Edited by T.Yamazaki
3. E.Karlisson, Physics Reports 82, 271 (1982)
4. K.Schroeder, Point Defects in Metal II. Springer Tracts in Modern Physics 87, 171 (1980). Contributions by P.H.Dederich, K.Schroeder and R.Zeller
5. A.I.Shirley and C.K.Hall, Acta Metall. 32, 985 (1983)
6. G.Leibfried and N.Breuer, Point Defect in Metal I. Springer Tracts in Modern Physics 81, (1978)
7. S.Estreicher and P.F.Meier (reference 1)  
Hyp. Int. 17-19, 241 (1984)
8. R.Kubo and T.Nagamiya, Solid State Physics. McGraw-Hill (1969)
9. N.Ashcroft and N.Mermin, Solid State Physics. Saunders College (1976)
10. H.A.Engel, Introduction to Nuclear Physics. Addison-Wesley (1966)
11. A.B.Denison, H.Graf, W.Kundig and P.F.Meier, Helvetica Physica Acta, 52, 460 (1979)
12. R.S.Hayano, Y.I.Uemura, J.Imazato, N.Nishida, T.Yamazaki and R.Kubo,  
Phys. Rev. 20B, 850 (1979)
13. T.Yamazaki, Hyp. Int. 6, 115 (1979)
14. C.Boekema, R.H.Heffner, R.L.Hutson, M.Leon, M.E. Schillaci, W.J.Kossler, M.Numan and S.A.Dodds.  
Phys. Rev. 26B, 2341 (1982)

15. M.Manninen, P.Hautojarvi and R.Nieminen.  
Solid State Commun. 23, 795 (1977)
16. C.Kittel, Introduction to Solid State Physics.  
Wiley (1967)
17. M.Namkung Ph.D. Thesis (College of William and Mary,  
1982) "A  $\mu$ SR Study of Uniaxial Stress Induced Symmetry  
Breaking in an Fe Single Crystal"
18. H.Peisl, Topics in Applied Physics (Hydrogen in Metal I)  
2A, 53 (1978). Edited by G.Alefeld and J.Volkl19.
19. W.J.Kossler, A.T.Fiory, W.F.Lankford, J.Lindemuth,  
K.G.Lynn, S.Mahajan, R.P.Minnich, K.G.Petzinger  
and C.E.Stronach  
Phys. Rev. Let. 41, 1558 (1978)
20. W.J.Kossler, A.T.Fiory, W.F.Lankford, K.G.Lynn,  
R.P.Minnich and C.E.Stronach  
Hyp. Int. 6, 295 (1979)
21. K.W.Kehr, D.Richter, J.M.Welter, O.Hartmann, E.Karlsson,  
L.O.Norlin, T.O.Niinikoski and A.Yaouanc  
Phys. Rev. 26B , 567 (1982)
22. W.B.Pearson, Handbook of Lattice Spacings and Structures  
of Metals.  
Pergamon Press 4 (1964)
23. P.R.Bevington, Data Reduction and Error Analysis for the  
Physical Sciences.  
McGraw-Hill, 235 (1969)
24. A.Seeger, (reference 1)  
Hyp. Int. 17-19, 75 (1984)
25. J.DeLaunay, Solid State Physics 2, 219 (1956)  
Edited by F.Seitz and D.Turnbull  
Academic Press
26. J.A.Brown, R.H.Heffner, M.Leon, M.E.Schillaci,  
D.W.Cooke and W.B.Gauster  
Phy. Rev. Let. 43 1513 (1979)
27. T.Hatano, Y.Suzuki, M.Doyama, Y.J.Uemura, T.Yamazaki  
and J.H.Brewer (reference 1)  
Hyp. Int. 17-19, 211 (1984)
28. H.Sugimoto and Y.Fukai,  
Phys. Rev. 22B, 670 (1980)

29. W.J.Kossler, M.Namkung, B.Hitti, Y.Li, J.Kempton, C.E.Stronach, L.R.Goode Jr., W.F.Lankford B.D.Patterson, W.Kundig and R.I.Grynszpan. Phys. Rev. 32B, 293 (1985)
30. J.Leese and A.E.Loard Jr. App. Phys. 39, 3986 (1968)
31. A.H.Morrish, The Physics Principles of Magnetism. Wiley (1965)
32. W.J.Carr Jr., in The Encyclopedia of Physics. Springer Vol. XVIII/2, 308 (1966)
33. P.Jena, M.Manninen, R.M.Nieminen and M.J.Puska. Phys. Rev. 29B, 4170 (1984)
34. T.Butz, J.Chappert, J.F.Dufrensne, O.Hartmann, E.Karleson, B.Lindgren, L.O.Norlin, P.Podini and A.Yaouanc. Phys. Lett. 75A, 321 (1980)
35. A.S.Nowick and B.S.Berry, Anelastic Relaxation in Crystalline Solids (Academic Press, New York 1972)

VITA

BASSAM SALIM HITTI

Date and Place of Birth:

Shemlan, Lebanon January 25 - 1960

Education:

B.S. (June 1981) American University of Beirut, M.S. (May 1983) and Ph.D. (May 1986) College of William and Mary.

Professional Employment:

Accepted a postdoctoral position at Eidgenossische Technische Hochschule Zurich.

Publication:

"Uniaxial Stress-Induced Symmetry Breaking for Muon Sites in Fe"  
W.J.Kossler, M.Namkung, B.Hitti, Y.Li, J.Kempton, C.E.Stronach, L.R.Goode Jr., W.F.Lankford, B.D.Batterson W.Kundig and R.I.Crynszpan.  
Phys. Rev. B 32, 293 (1985)

Manuscripts:

"Muon Diffusion and Trapping in Al-Impurity Alloys"  
W.J.Kossler, B.Hitti, J.Kempton, Y.Li, C.E.Stronach, W.F.Lankford and A.T.Flory.  
(to be submitted to Phys. Rev. B)

"Transverse and Longitudinal depolarization of Muons in TiHx"  
W.J.Kossler, H.Schone, B.Hitti, J.Kempton, Y.Li, C.E.Stronach, W.F.Lankford, J.Reilly and E.Seymour.  
(to be submitted to Phys. Rev. B)